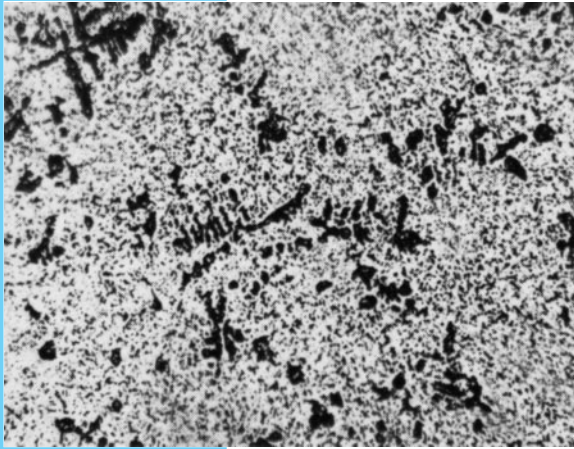
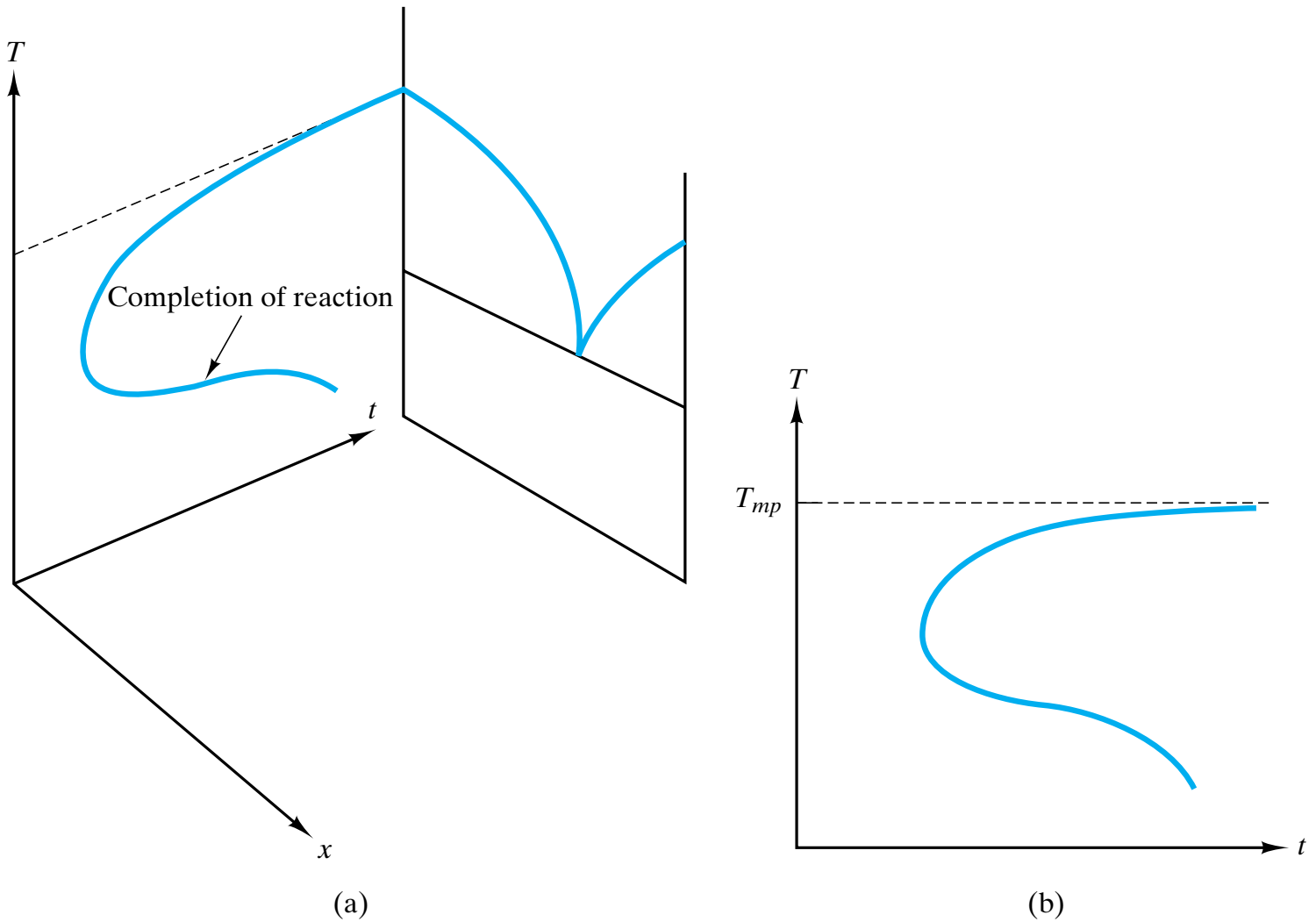


# CHAPTER 10

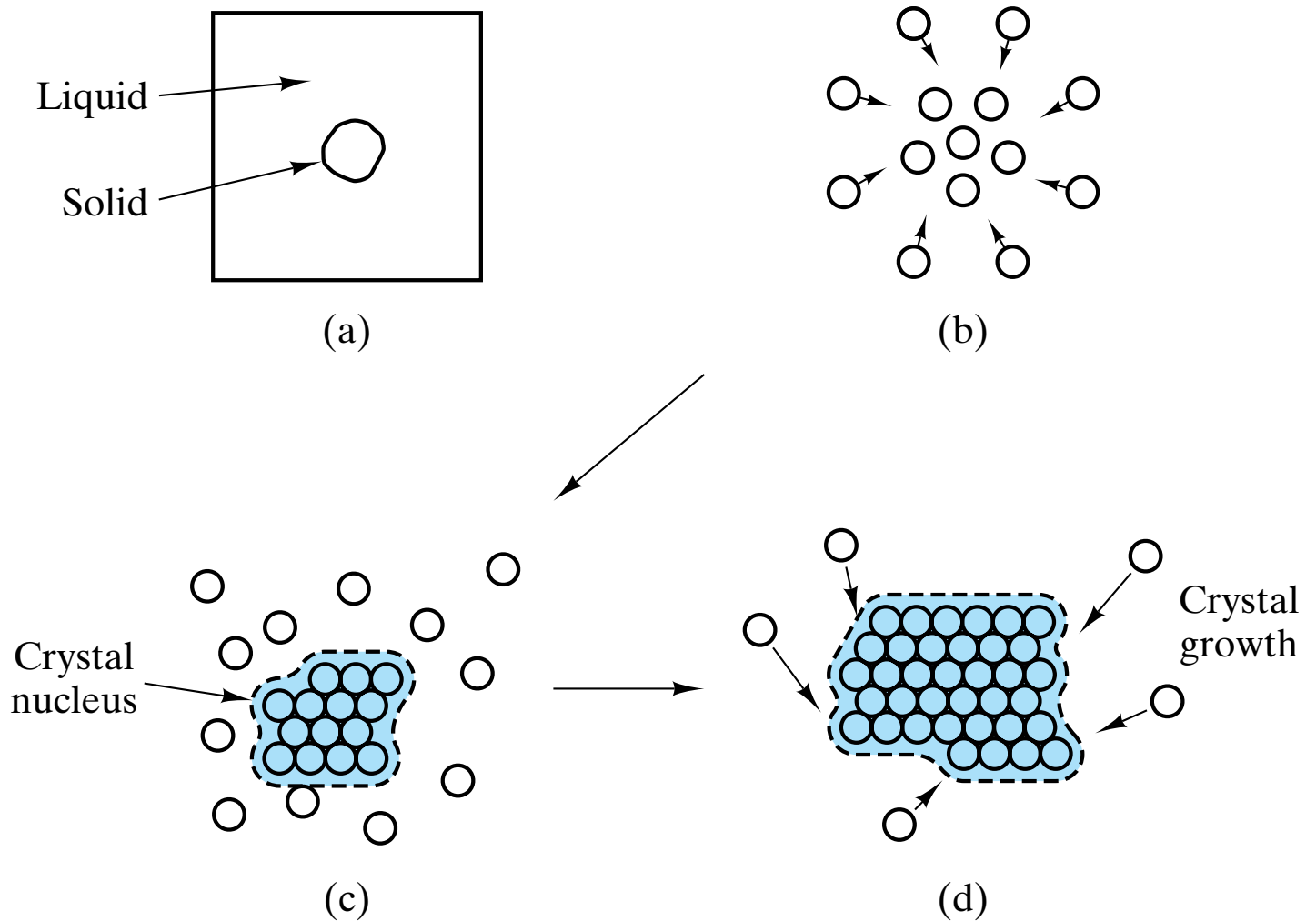
## Kinetics—Heat Treatment



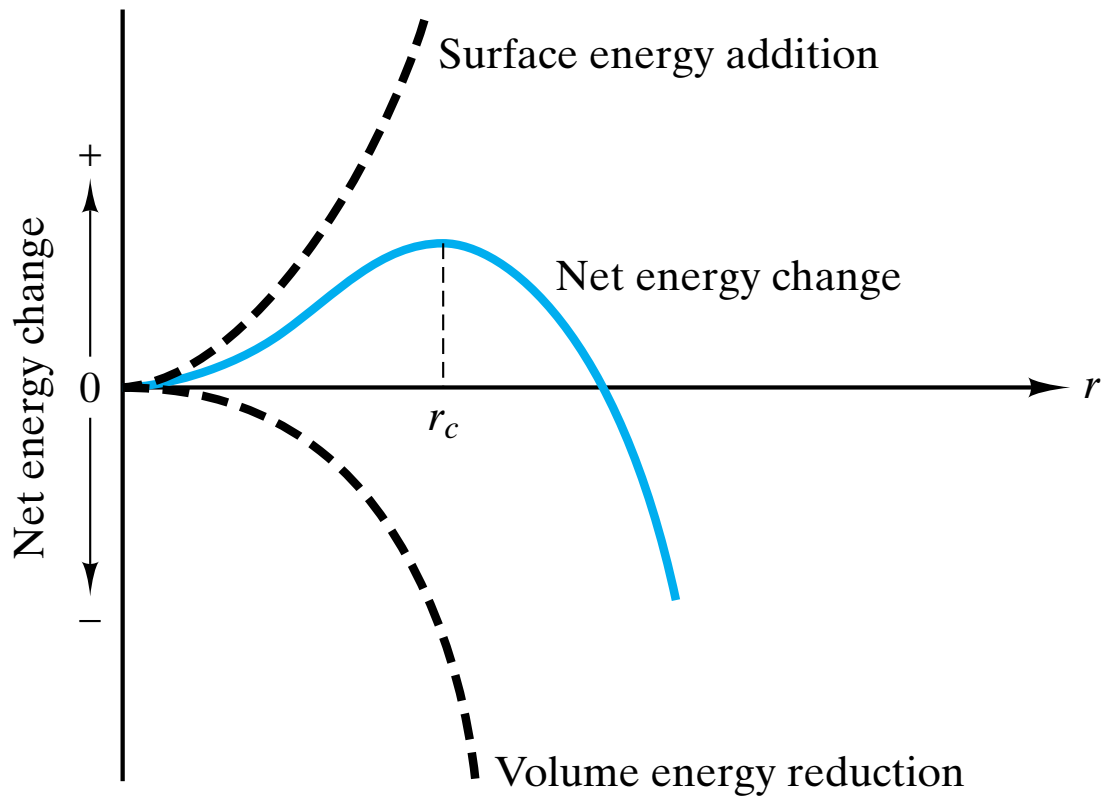
*The microstructure of a rapidly cooled “eutectic” soft solder ( $\approx 38$  wt % Pb – 62 wt % Sn) consists of globules of lead-rich solid solution (dark) in a matrix of tin-rich solid solution (white), 375X. The contrast to the slowly-cooled microstructure at the opening of Chapter 9 illustrates the effect of time on microstructural development. (From ASM Handbook, Vol. 3: Alloy Phase Diagrams, ASM International, Materials Park, Ohio, 1992.)*



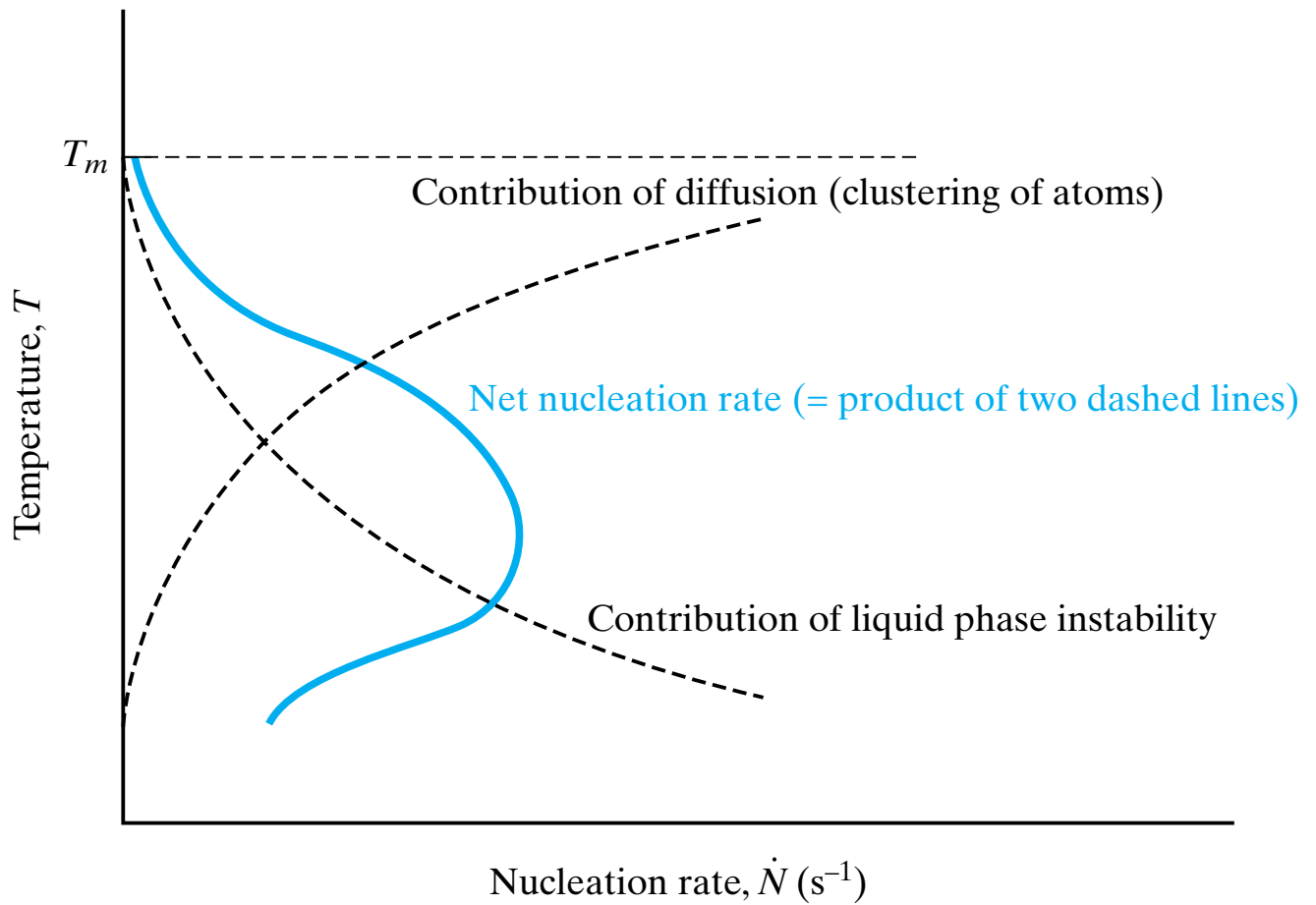
**Figure 10-1** Schematic illustration of the approach to equilibrium. (a) The time for solidification to go to completion is a strong function of temperature, with the minimum time occurring for a temperature considerably below the melting point. (b) The temperature-time plane with “transformation curve.” We shall see later that the time axis is often plotted on a logarithmic scale.



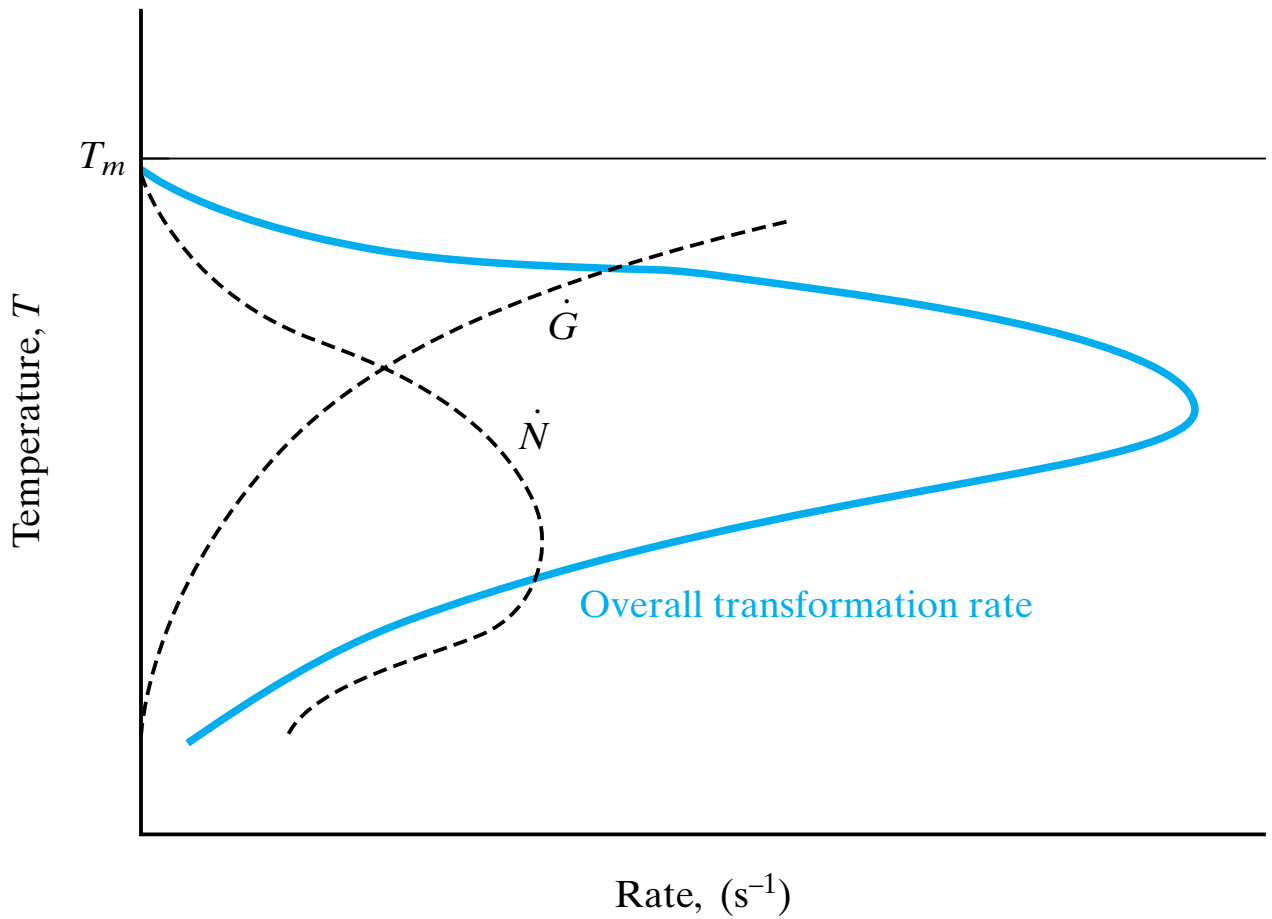
**Figure 10-2** (a) On a microscopic scale, a solid precipitate in a liquid matrix. The precipitation process is seen on the atomic scale as (b) a clustering of adjacent atoms to form (c) a crystalline nucleus followed by (d) the growth of the crystalline phase.



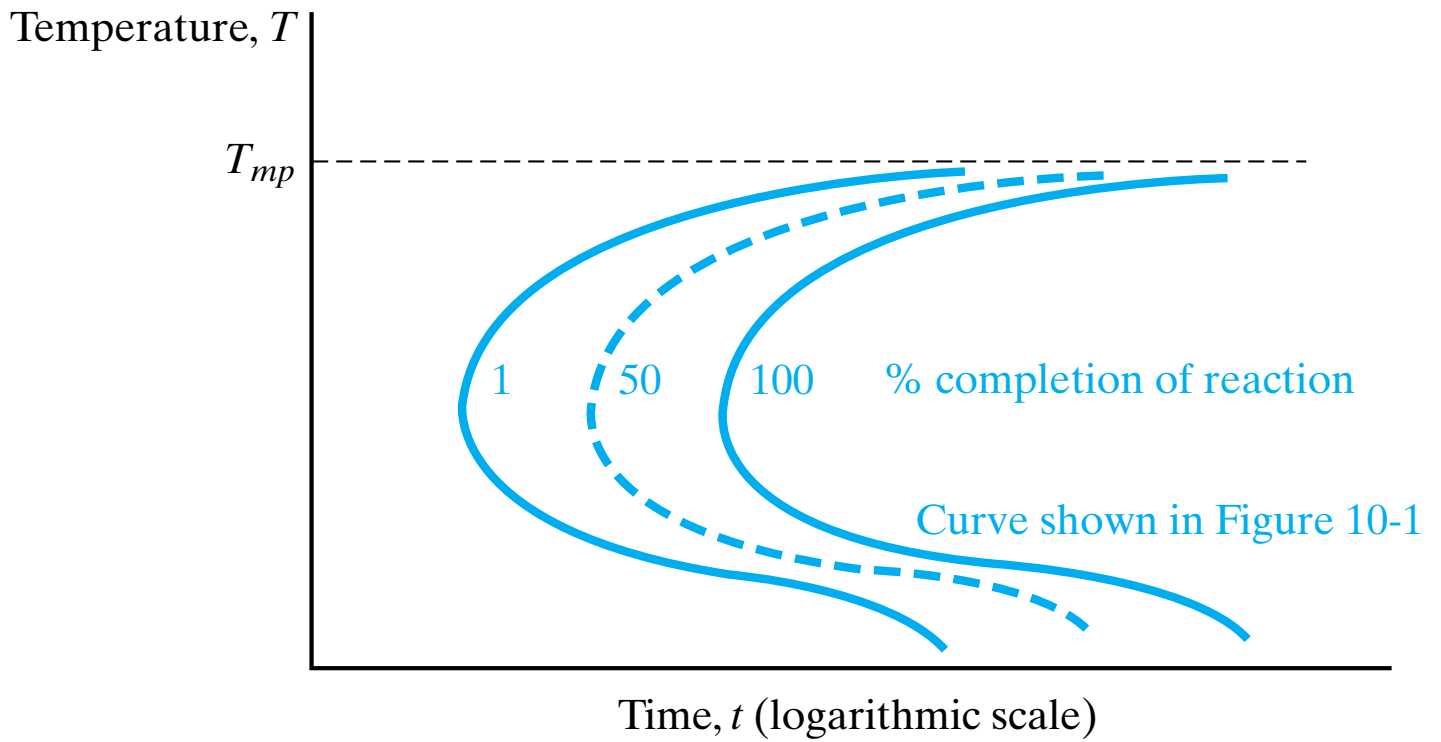
**Figure 10-3** *Classical nucleation theory involves an energy balance between the nucleus and its surrounding liquid. A nucleus (cluster of atoms) as shown in Figure 10–2(c) will be stable only if further growth reduces the net energy of the system. An ideally spherical nucleus will be stable if its radius,  $r$ , is greater than a critical value,  $r_c$ .*



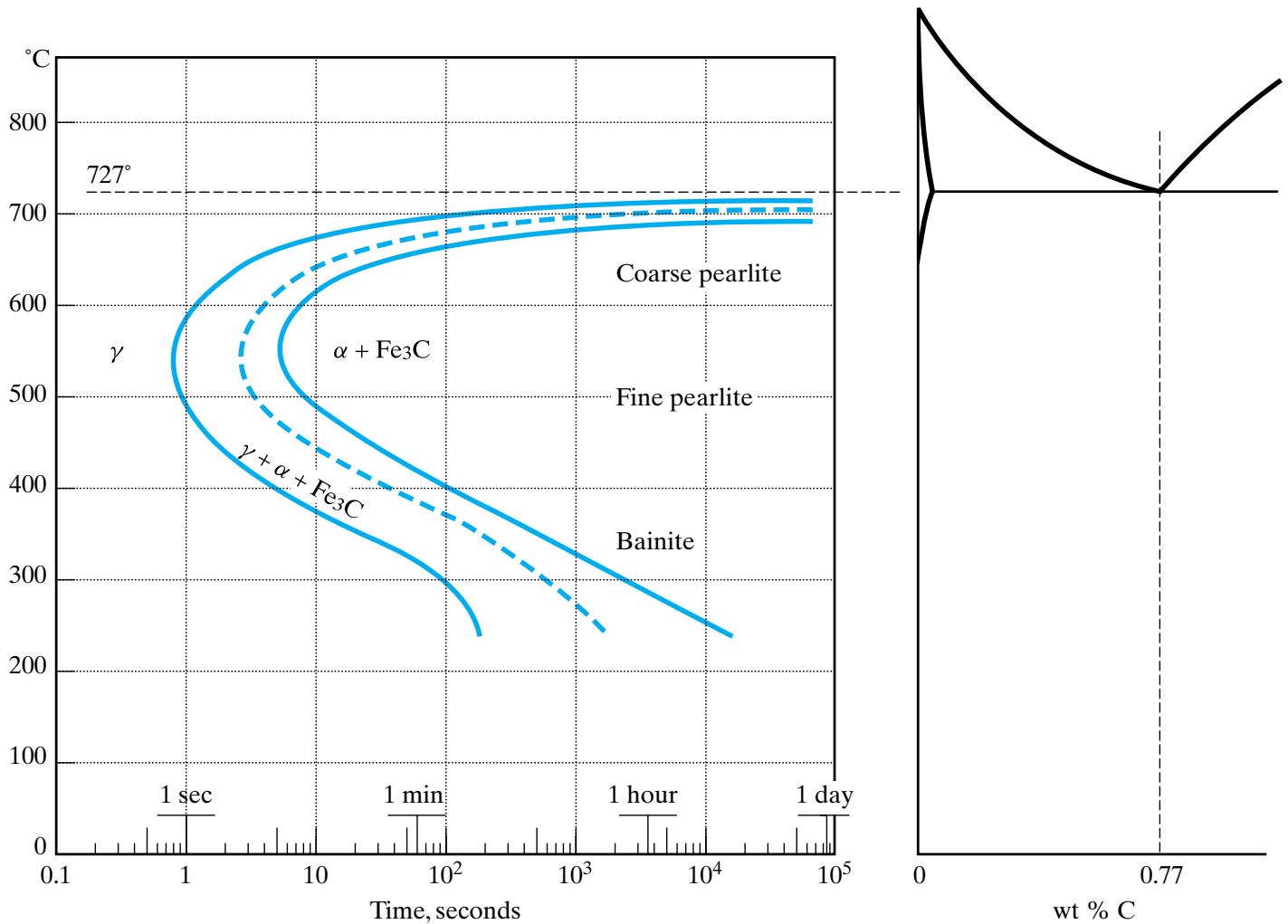
**Figure 10-4** *The rate of nucleation is a product of two curves that represent two opposing factors (instability and diffusivity).*



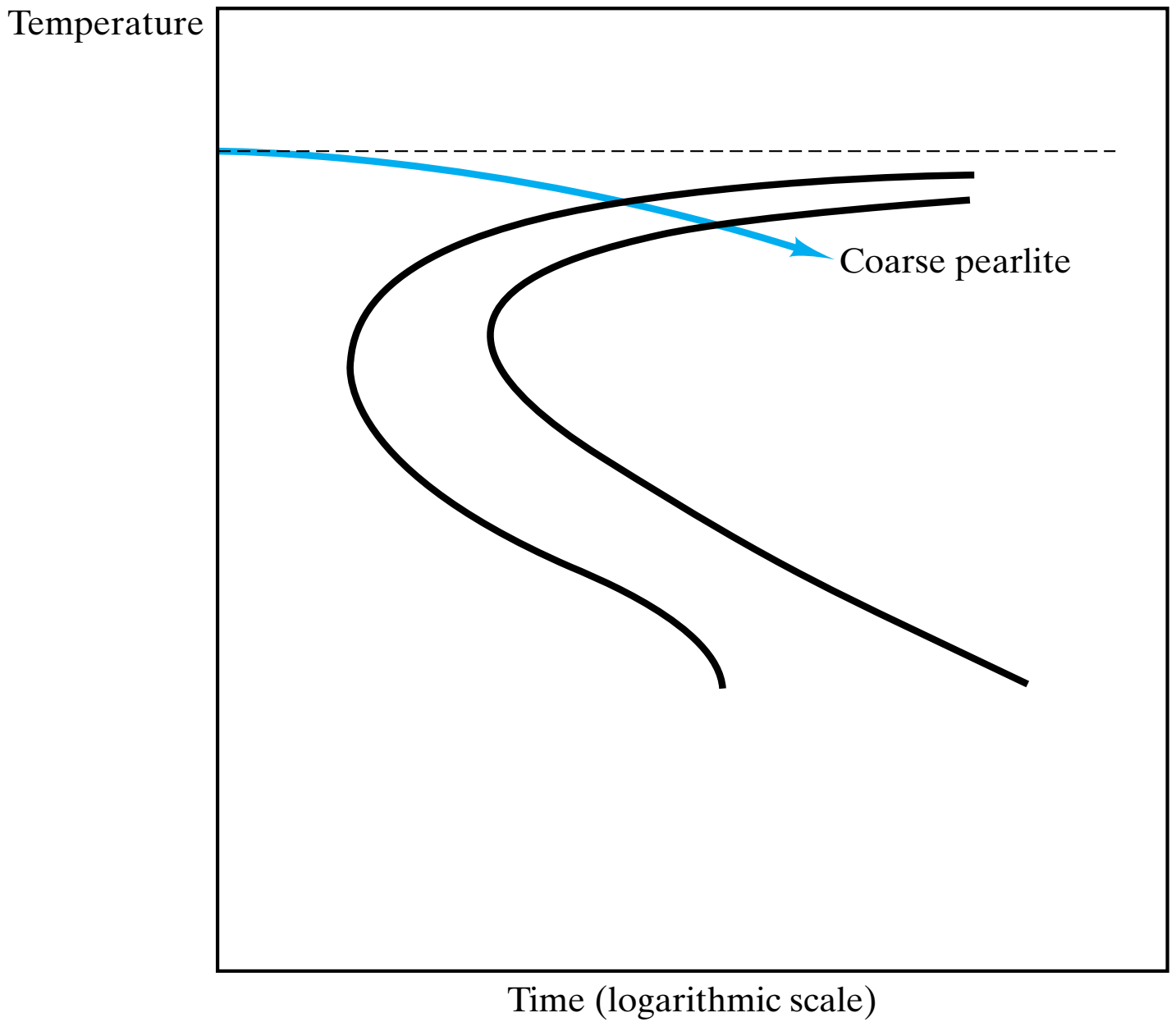
**Figure 10-5** The overall transformation rate is the product of the nucleation rate  $\dot{N}$  (from Figure 10-4) and the growth rate  $\dot{G}$  (given by Equation 10.1).



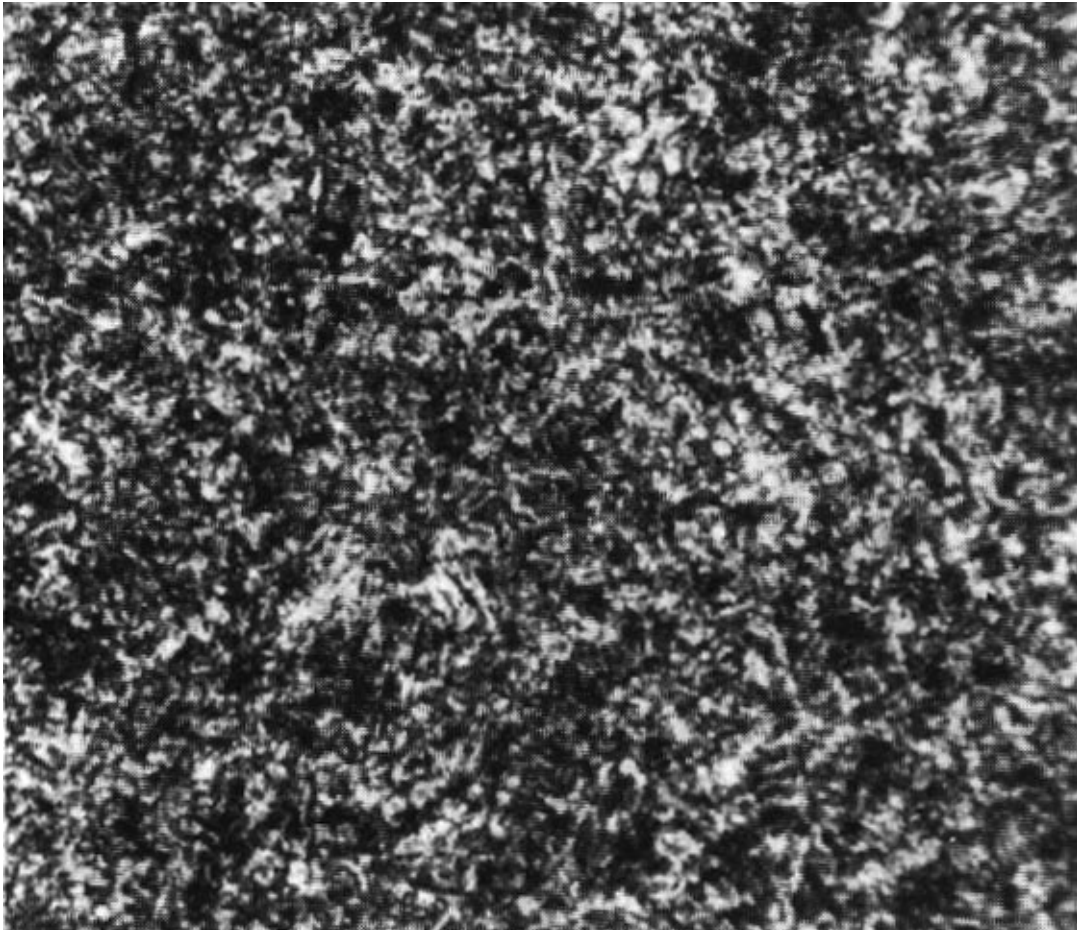
**Figure 10-6** A time-temperature-transformation diagram for the solidification reaction of Figure 10-1 with various percent completion curves illustrated.



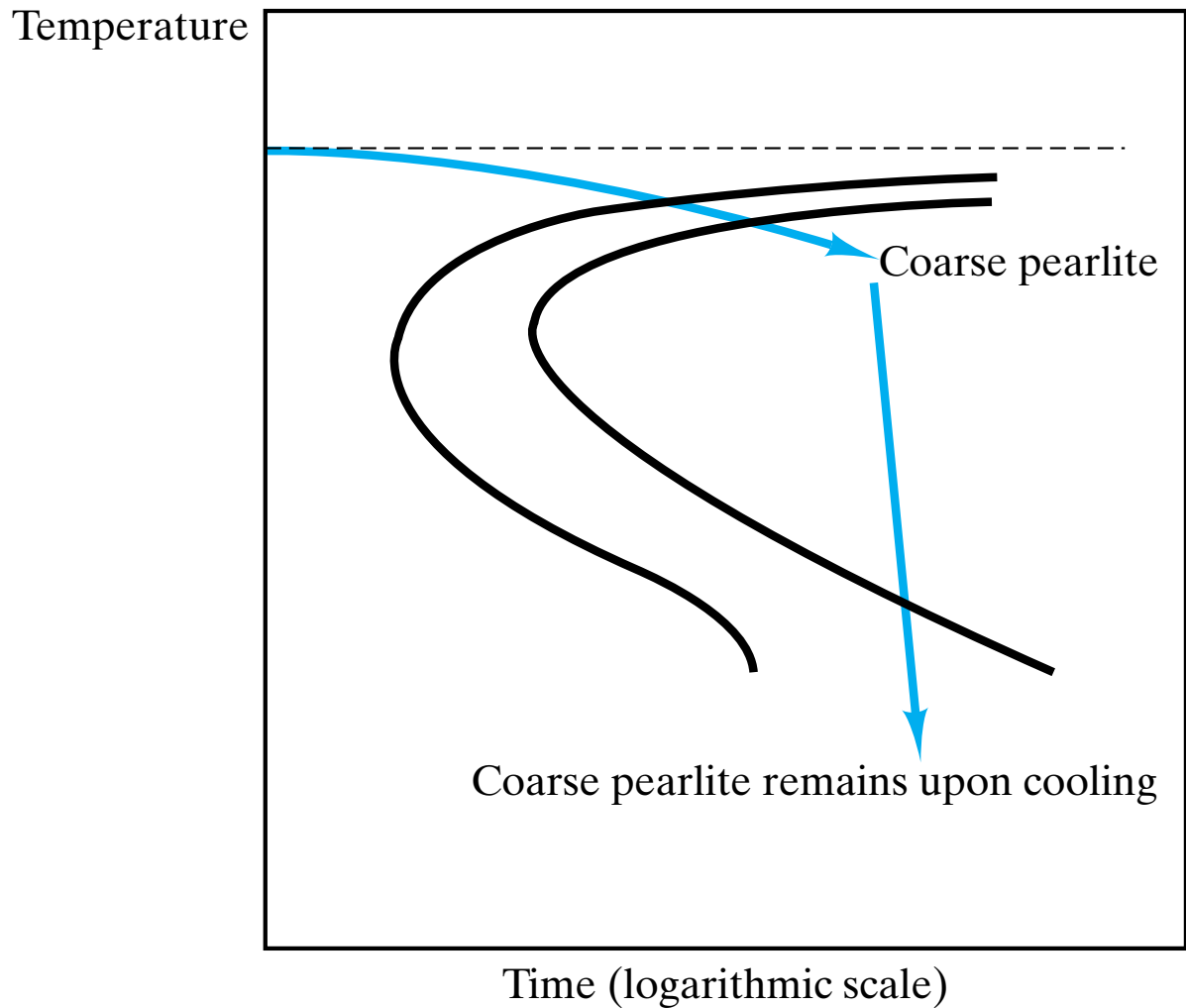
**Figure 10-7** TTT diagram for eutectoid steel shown in relation to the Fe–Fe<sub>3</sub>C phase diagram (see Figure 9–39). This shows that, for certain transformation temperatures, bainite rather than pearlite is formed. In general, the transformed microstructure is increasingly fine-grained as the transformation temperature is decreased. Nucleation rate increases and diffusivity decreases as temperature decreases. The solid curve on the left represents the onset of transformation (~ 1% completion). The dashed curve represents 50% completion. The solid curve on the right represents the effective (~ 99%) completion of transformation. This convention is used in subsequent TTT diagrams. (TTT diagram after Atlas of Isothermal Transformation and Cooling Transformation Diagrams, American Society for Metals, Metals Park, Ohio, 1977.)



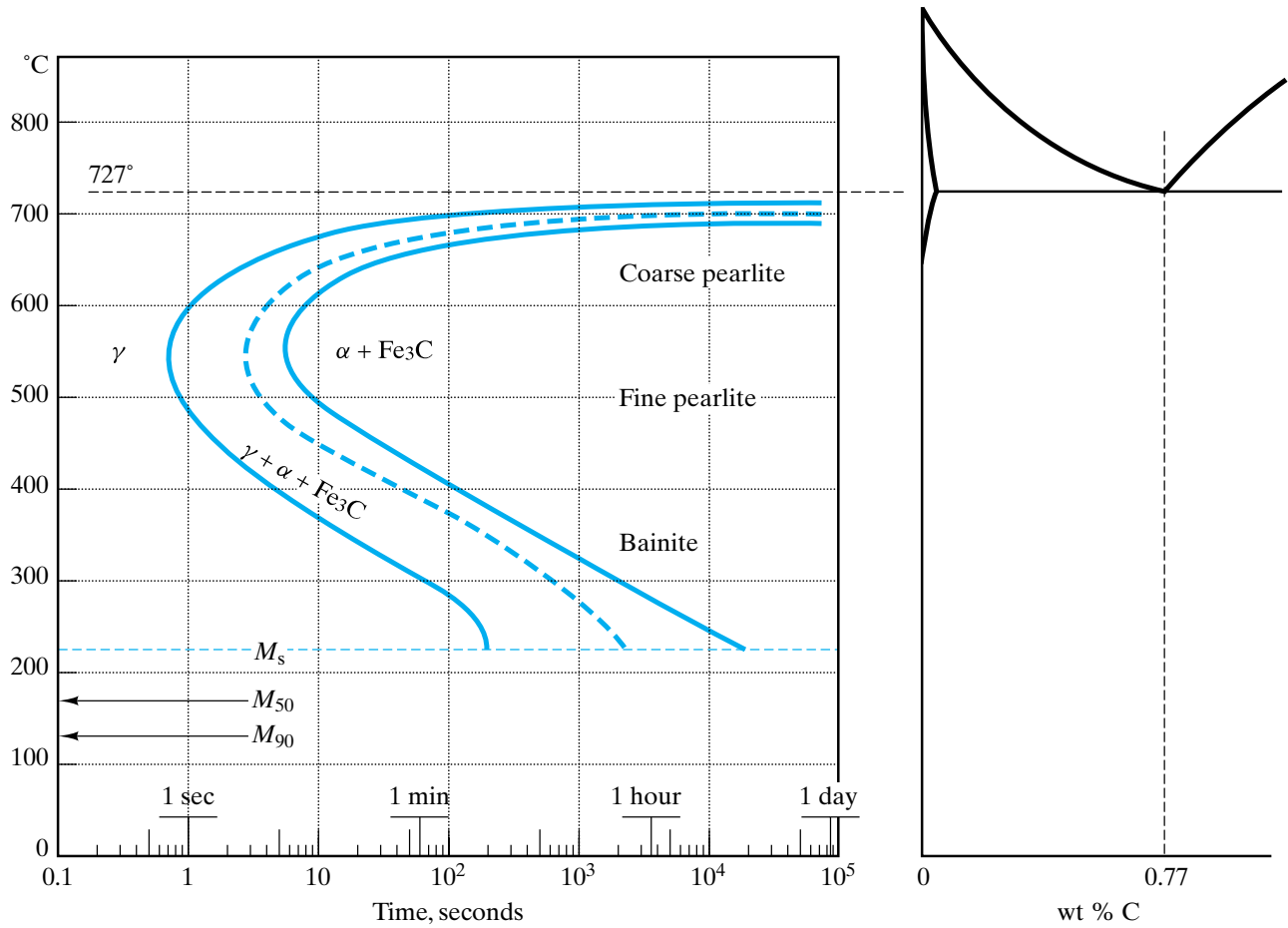
**Figure 10-8** A slow cooling path that leads to coarse pearlite formation is superimposed on the TTT diagram for eutectoid steel. This type of thermal history was assumed, in general, throughout Chapter 9.



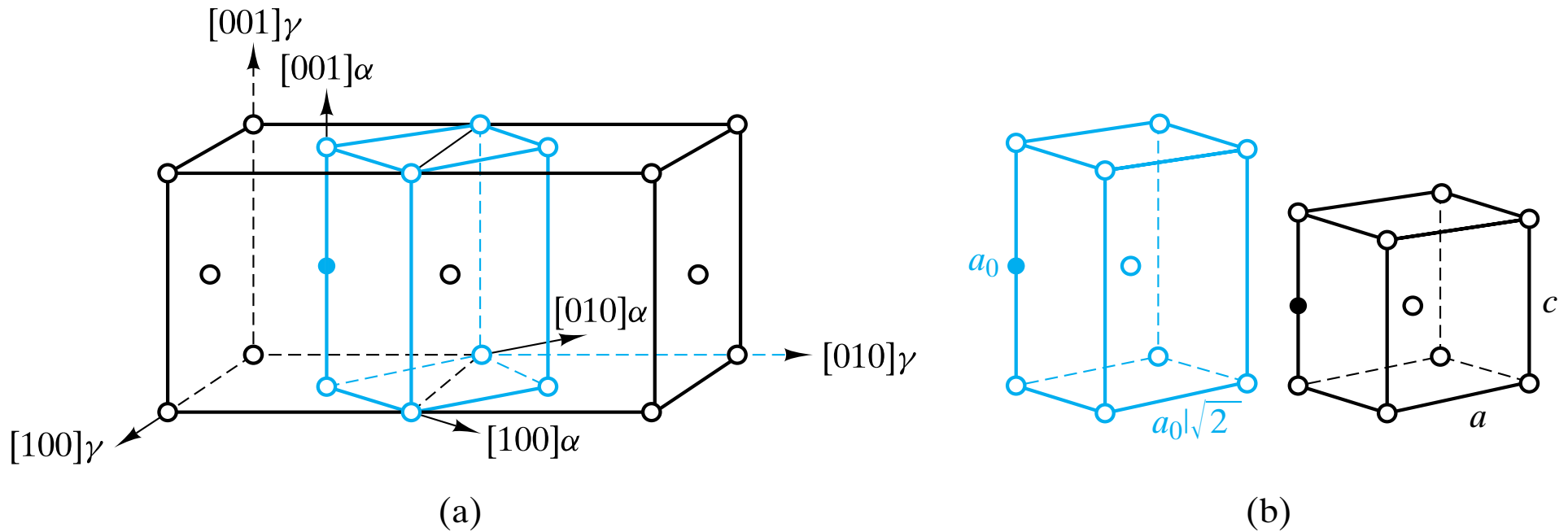
**Figure 10-9** *The microstructure of bainite involves extremely fine needles of  $\alpha$ -Fe and  $Fe_3C$ , in contrast to the lamellar structure of pearlite (see Figure 9-2), 535 $\times$ . (From Metals Handbook, 8th Ed., Vol. 7: Atlas of Microstructures, American Society for Metals, Metals Park, Ohio, 1972.)*



**Figure 10-10** *The interpretation of TTT diagrams requires consideration of the thermal history “path.” For example, coarse pearlite, once formed, remains stable upon cooling. The finer-grain structures are less stable because of the energy associated with the grain boundary area. (By contrast, phase diagrams represent equilibrium and identify stable phases independent of the path used to reach a given state point.)*



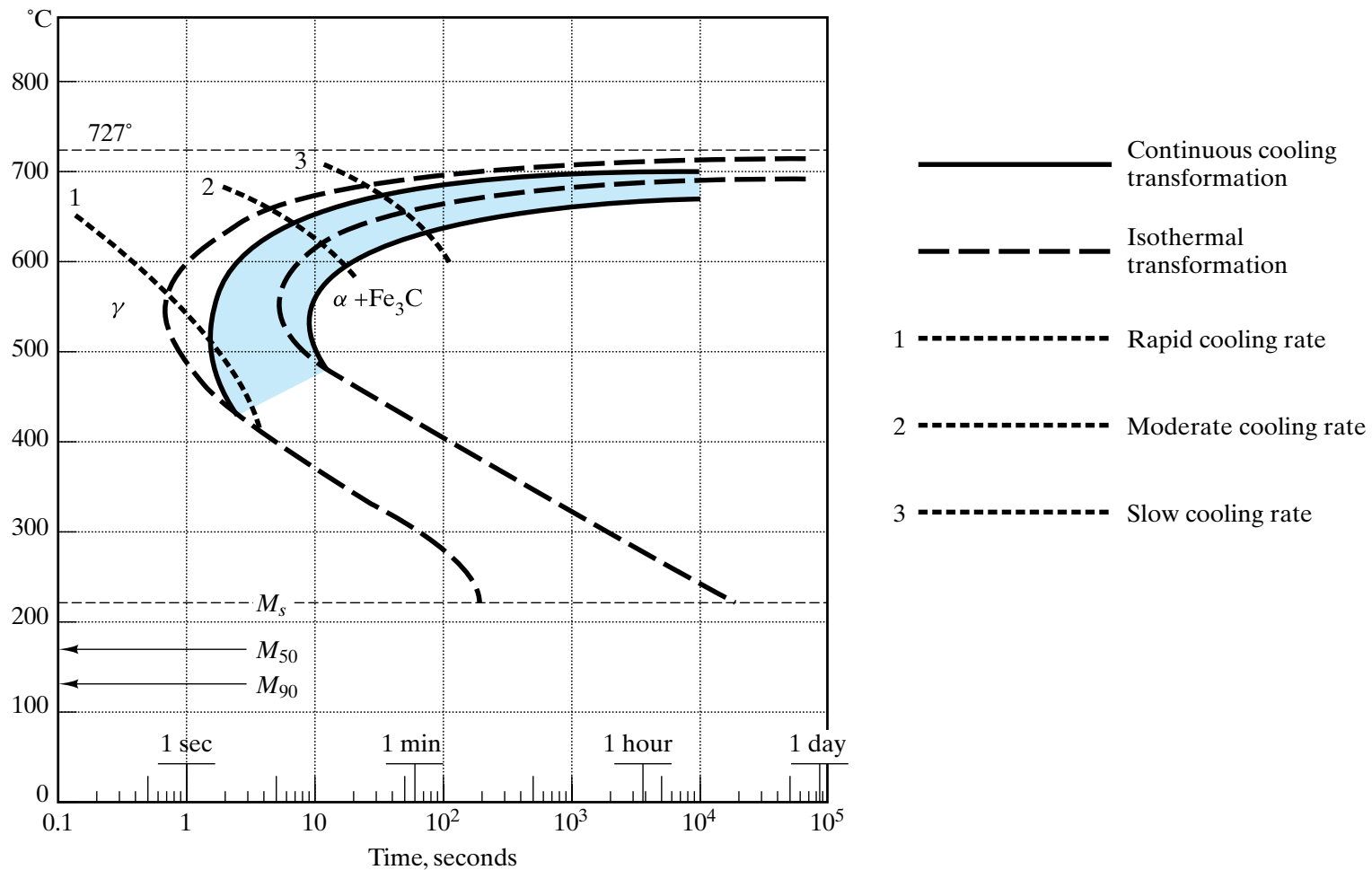
**Figure 10-11** A more complete TTT diagram for eutectoid steel than was given in Figure 10-7. The various stages of the time-independent (or diffusionless) martensitic transformation are shown as horizontal lines.  $M_s$  represents the start,  $M_{50}$  50% transformation, and  $M_{90}$  90% transformation. One hundred percent transformation to martensite is not complete until a final temperature ( $M_f$ ) of  $-46^\circ C$ .



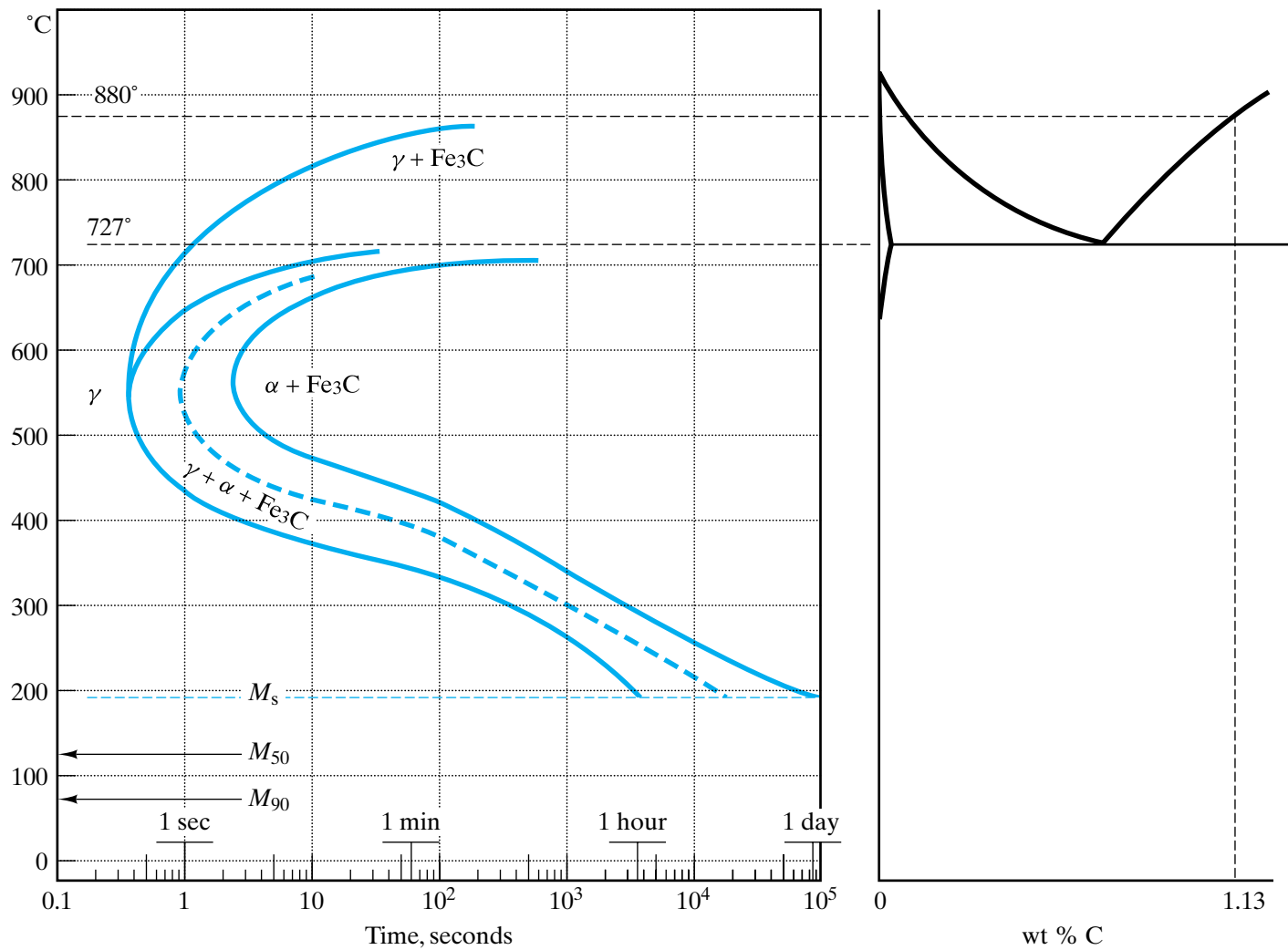
**Figure 10-12** For steels, the martensitic transformation involves the sudden reorientation of C and Fe atoms from the fcc solid solution of  $\gamma$ -Fe (austenite) to a body-centered tetragonal (bct) solid solution (martensite). In (a), the bct unit cell is shown relative to the fcc lattice by the  $\langle 100 \rangle_{\alpha}$  axes. In (b), the bct unit cell is shown before (left) and after (right) the transformation. The open circles represent iron atoms. The solid circle represents an interstitially dissolved carbon atom. This illustration of the martensitic transformation was first presented by Bain in 1924, and while subsequent study has refined the details of the transformation mechanism, this remains a useful and popular schematic. (After J. W. Christian, in *Principles of Heat Treatment of Steel*, G. Krauss, Ed., American Society for Metals, Metals Park, Ohio, 1980.)



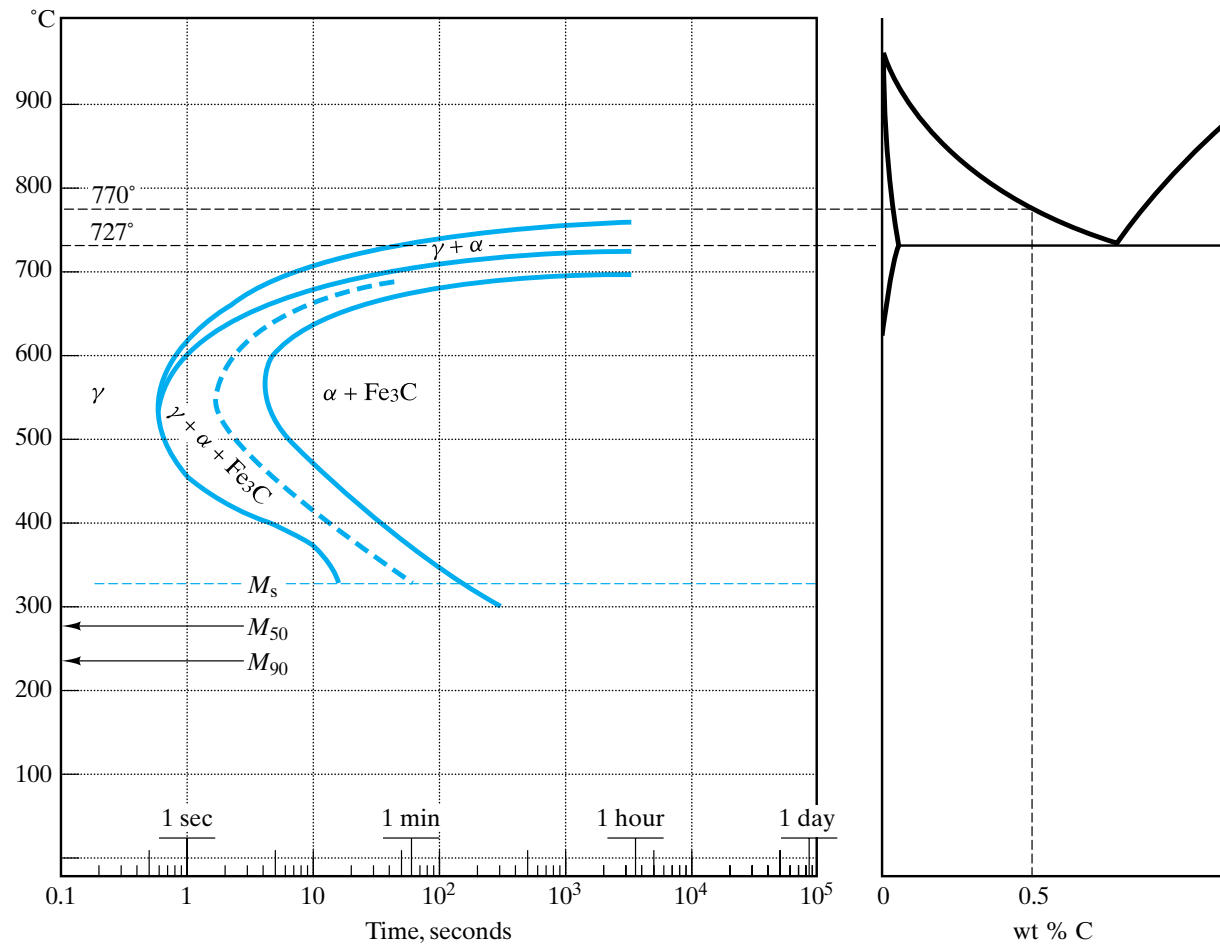
**Figure 10-13** *Acicular, or needlelike, microstructure of martensite 1000 $\times$ . (From Metals Handbook, 8th Ed., Vol. 7: Atlas of Microstructures, American Society for Metals, Metals Park, Ohio, 1972.)*



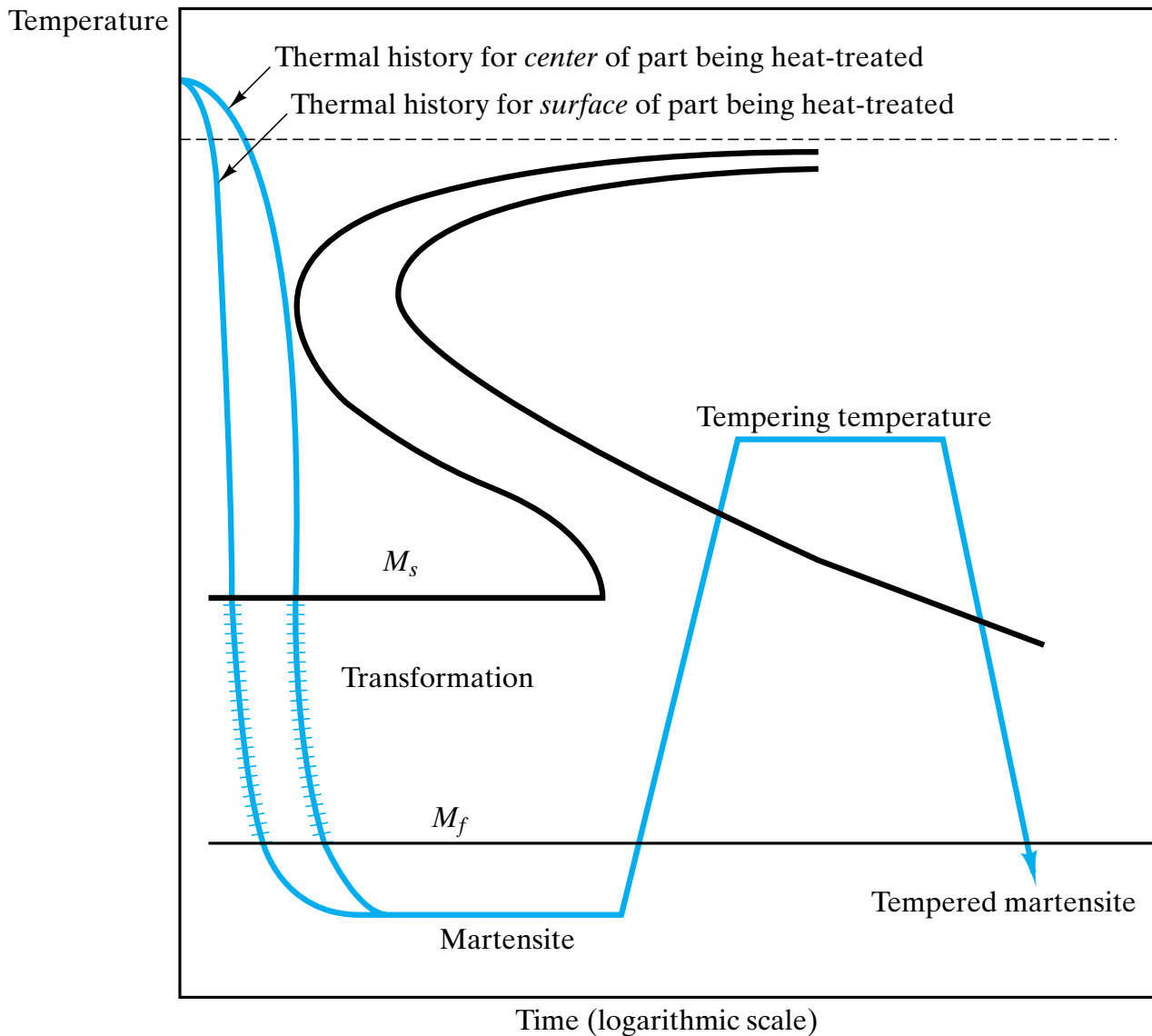
**Figure 10-14** A continuous cooling transformation (CCT) diagram is shown superimposed on the isothermal transformation diagram of Figure 10-11. The general effect of continuous cooling is to shift the transformation curves downward and toward the right. (After Atlas of Isothermal Transformation and Cooling Transformation Diagrams, American Society for Metals, Metals Park, Ohio, 1977.)



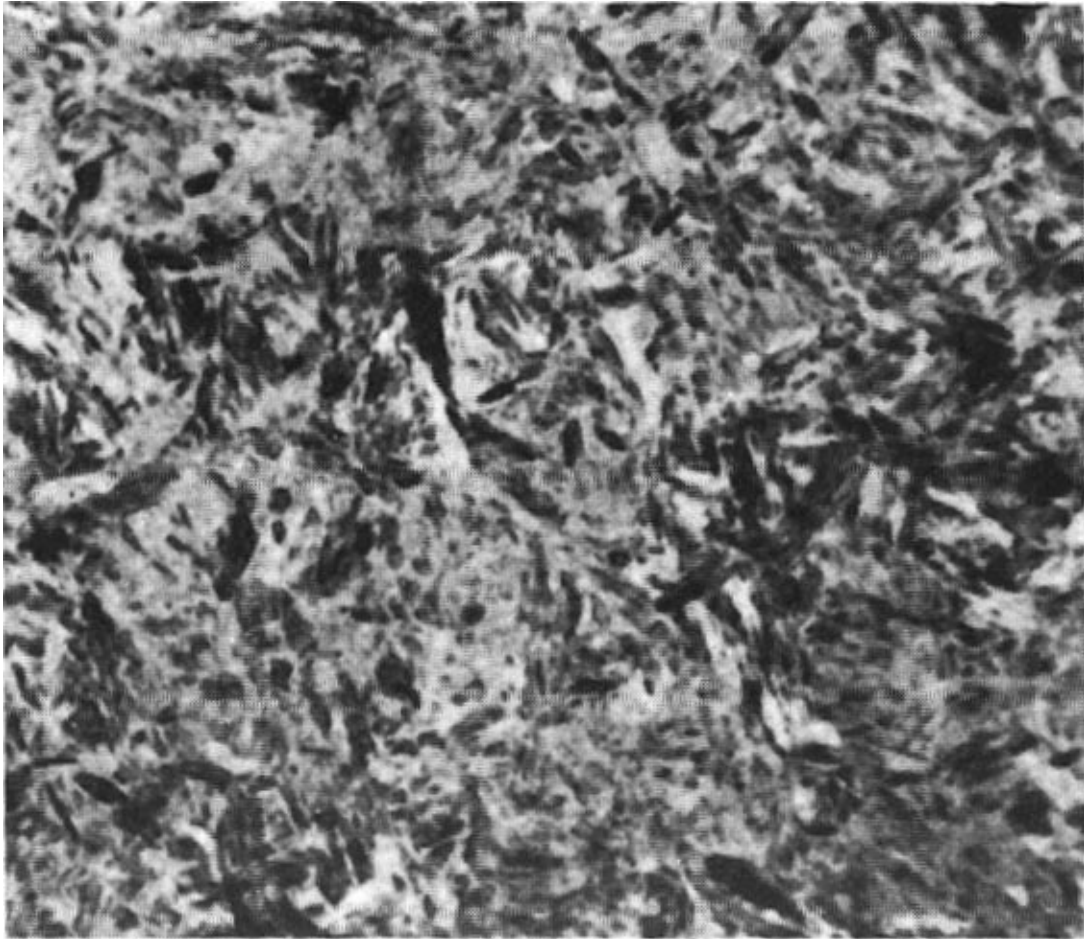
**Figure 10-15** TTT diagram for a hypereutectoid composition (1.13 wt % C) compared to the Fe-Fe<sub>3</sub>C phase diagram. Microstructural development for the slow cooling of this alloy was shown in Figure 9-40. (TTT diagram after Atlas of Isothermal Transformation and Cooling Transformation Diagrams, American Society for Metals, Metals Park, Ohio, 1977.)



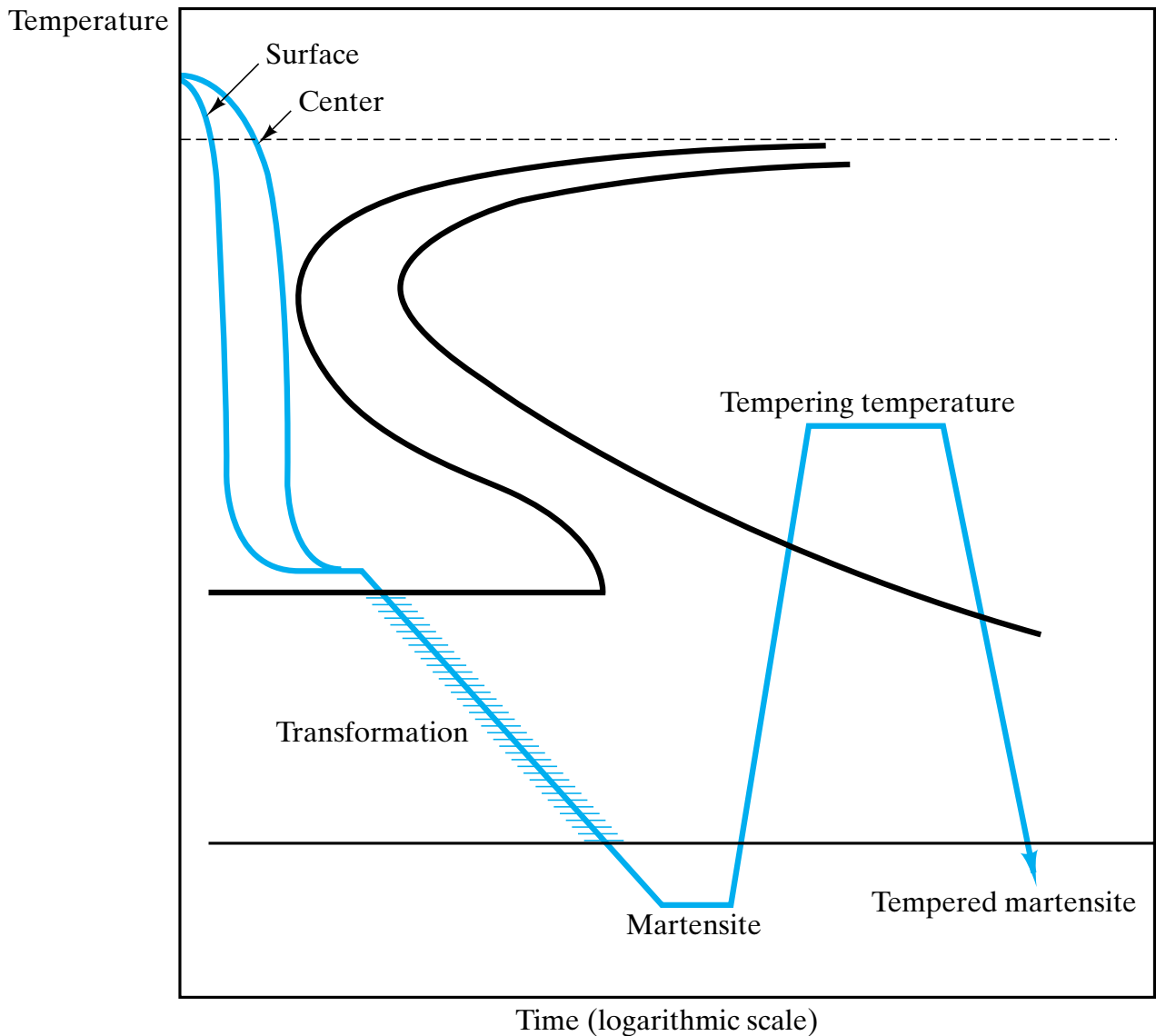
**Figure 10-16** TTT diagram for a hypo-eutectoid composition (0.5 wt % C) compared to the Fe-Fe<sub>3</sub>C phase diagram. Microstructural development for the slow cooling of this alloy was shown in Figure 9-41. By comparing Figures 10-11, 10-15, and 10-16, one will note that the martensitic transformation occurs at decreasing temperatures with increasing carbon content in the region of the eutectoid composition. (TTT diagrams after Atlas of Isothermal Transformation and Cooling Transformation Diagrams, American Society for Metals, Metals Park, Ohio, 1977.)



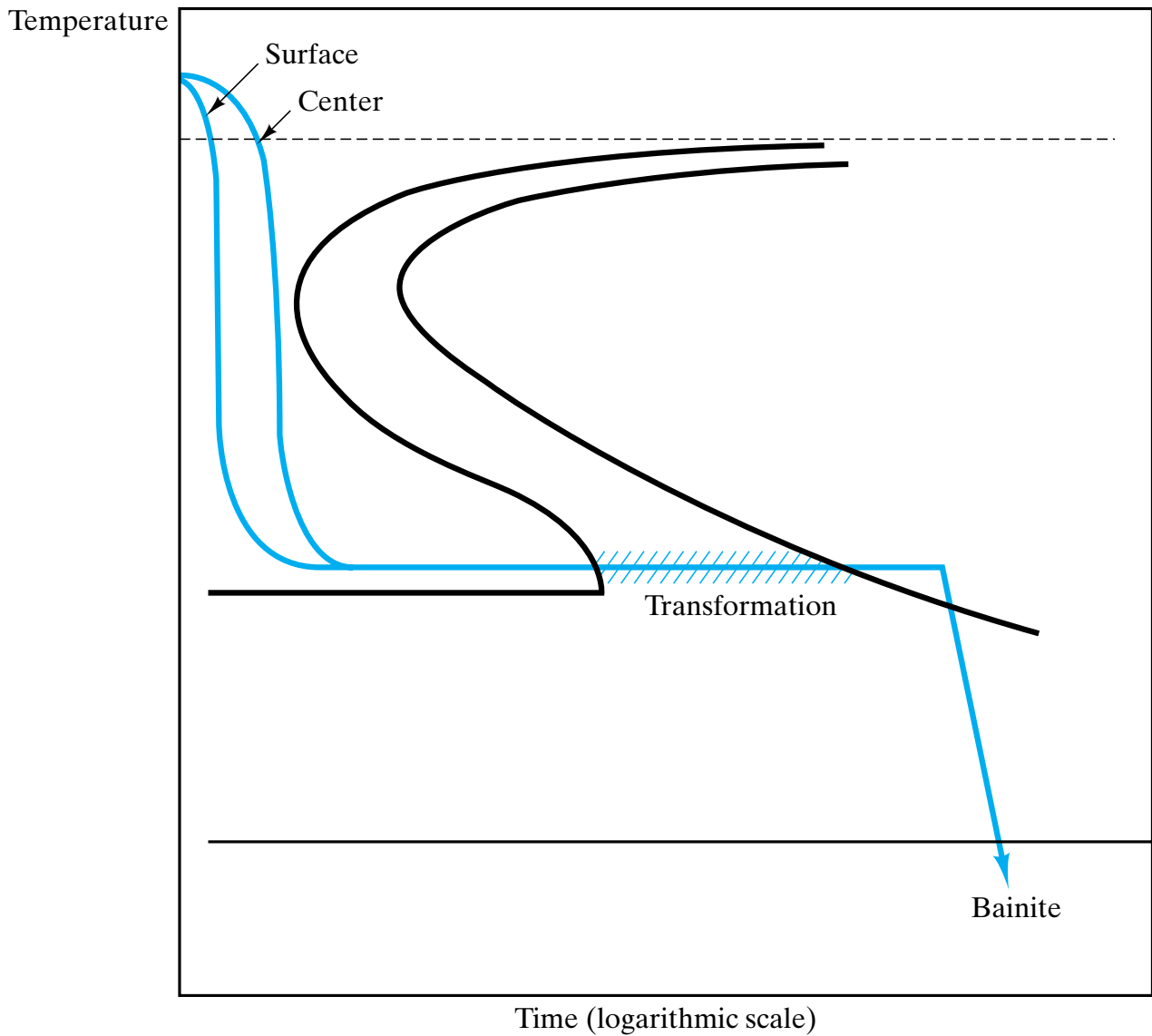
**Figure 10-17** Tempering is a thermal history [ $T = f_n(t)$ ] in which martensite, formed by quenching austenite, is reheated. The resulting tempered martensite consists of the equilibrium phase of  $\alpha$ -Fe and  $Fe_3C$  but in a microstructure different from both pearlite and bainite (note Figure 10-18). (After Metals Handbook, 8th Ed., Vol. 2, American Society for Metals, Metals Park, Ohio, 1964. It should be noted that the TTT diagram is, for simplicity, that of eutectoid steel. As a practical matter, tempering is generally done in steels with slower diffusional reactions permitting less severe quenches.)



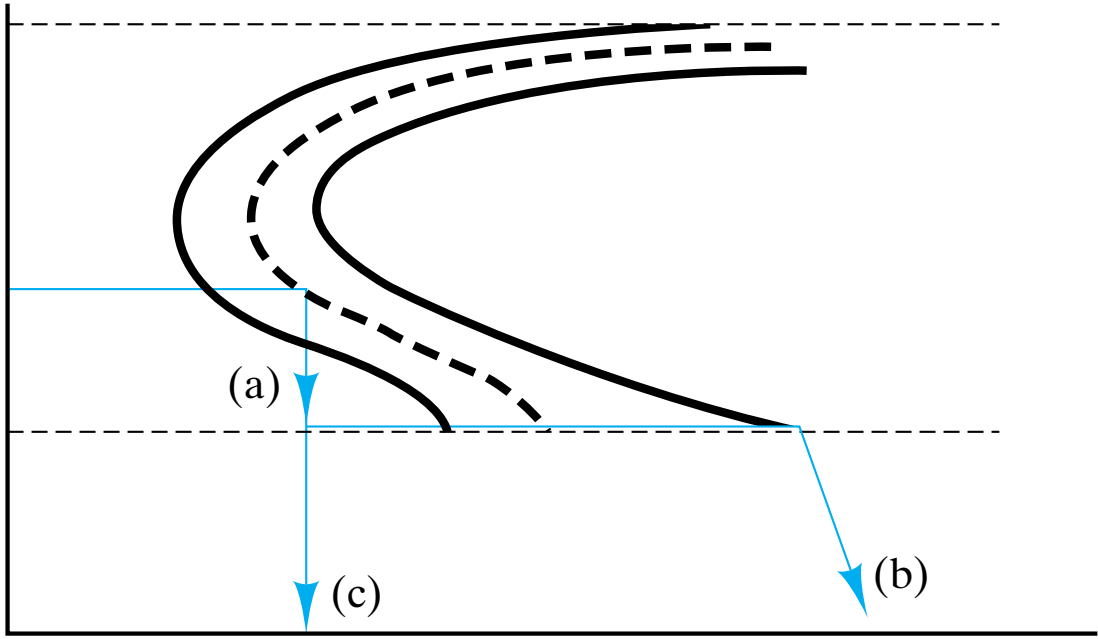
**Figure 10-18** *The microstructure of tempered martensite, although an equilibrium mixture of  $\alpha$ -Fe and  $Fe_3C$ , differs from those for pearlite (Figure 9-2) and bainite (Figure 10-9), 825 $\times$ . This particular microstructure is for a 0.50 wt % C steel comparable with that described for Figure 10-16. (From Metals Handbook, 8th Ed., Vol. 7: Atlas of Microstructures, American Society for Metals, Metals Park, Ohio, 1972.)*

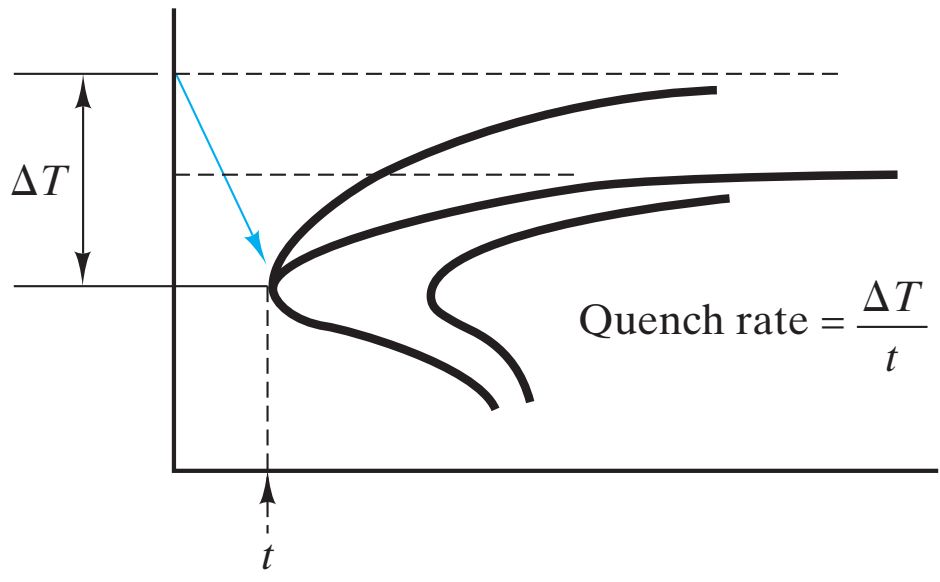


**Figure 10-19** *In martempering, the quench is stopped just above  $M_s$ . Slow cooling through the martensitic transformation range reduces stresses associated with the crystallographic change. The final reheat step is equivalent to that in conventional tempering. (After Metals Handbook, 8th Ed., Vol. 2, American Society for Metals, Metals Park, Ohio, 1964.)*



**Figure 10-20** *As with martempering, austempering avoids the distortion and cracking associated with quenching through the martensitic transformation range. In this case, the alloy is held long enough just above  $M_s$  to allow full transformation to bainite. (After Metals Handbook, 8th Ed., Vol. 2, American Society for Metals, Metals Park, Ohio, 1964.)*





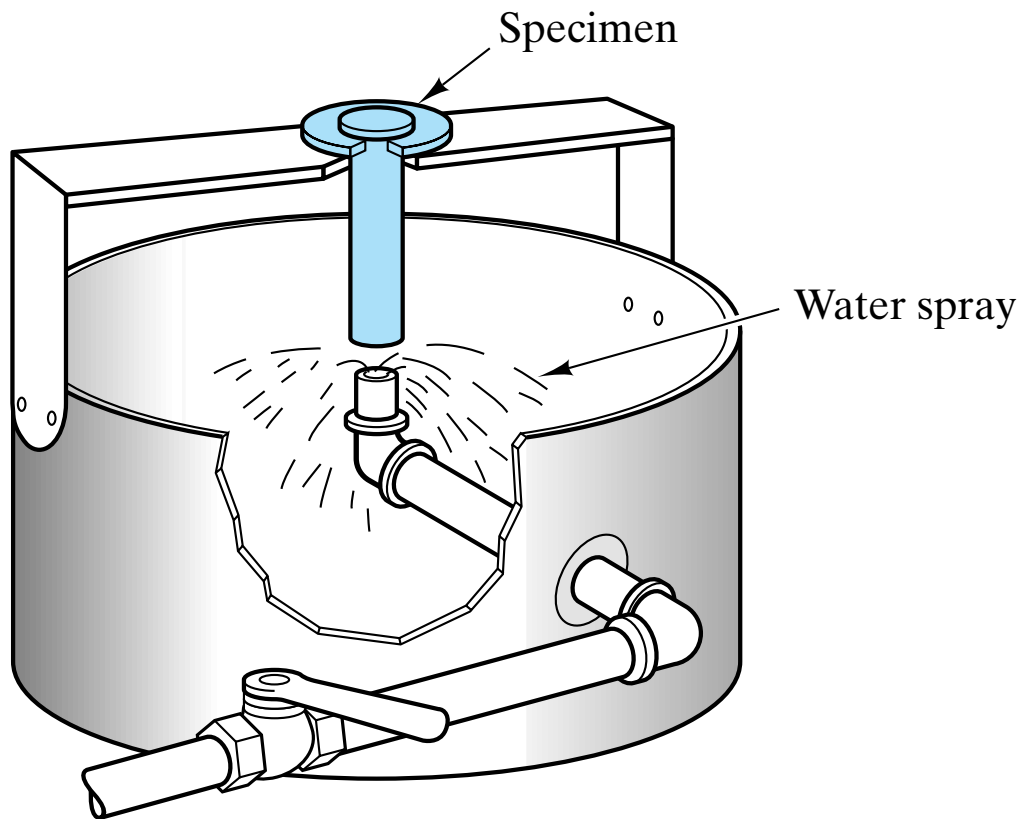


**Figure 10-21** *Schematic illustration of the Jominy end-quench test for hardenability. (After W. T. Lankford et al., Eds., The Making, Shaping, and Treating of Steel, 10th Ed., United States Steel, Pittsburgh, Pa., 1985. Copyright 1985 by United States Steel Corporation.)*

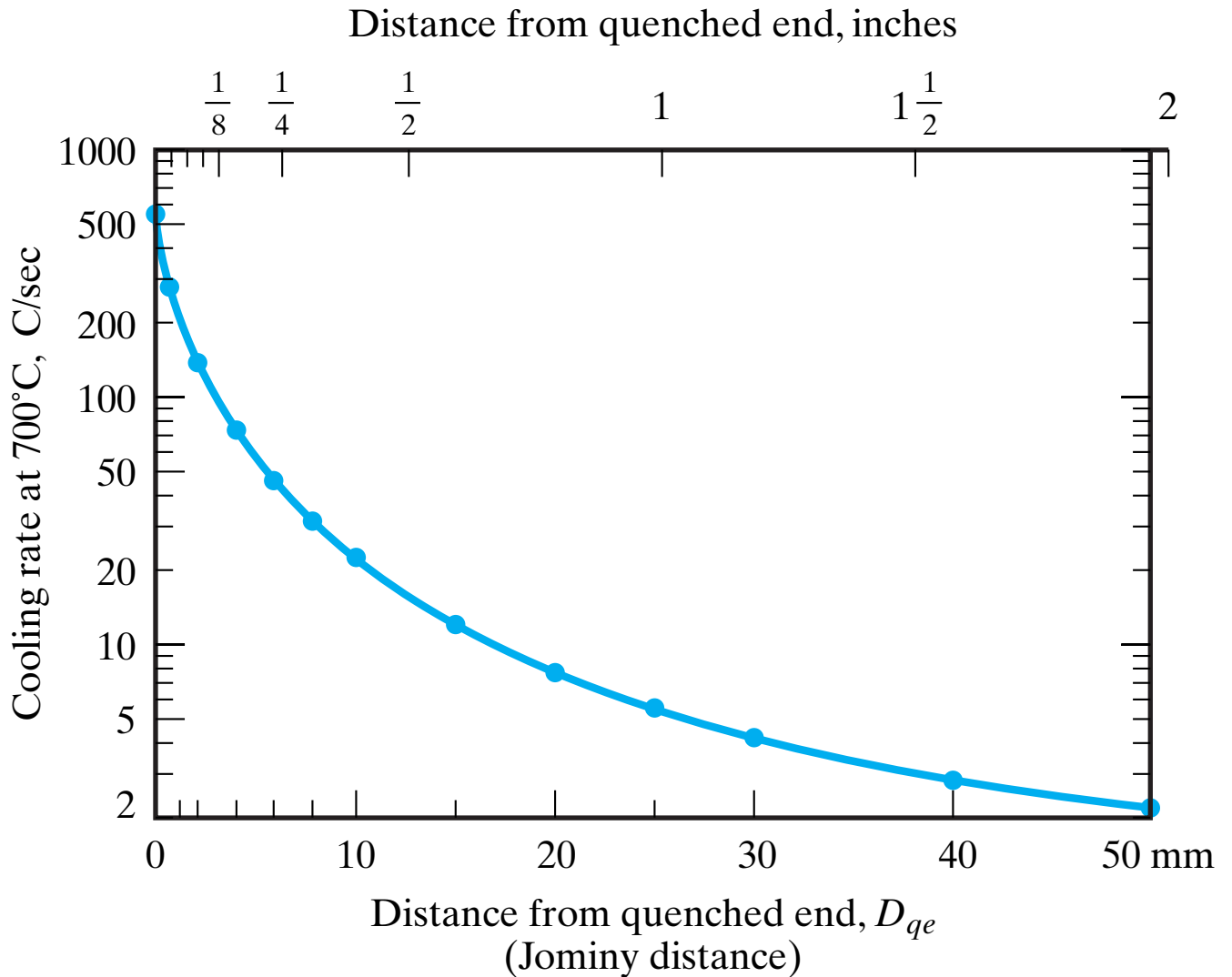


**Figure 10-22** The cooling rate for the Jominy bar (see Figure 10-21) varies along its length. This curve applies to virtually all carbon and low-alloy steels. (After L. H. Van Vlack, *Elements of Materials Science and Engineering, 4th Ed.*, Addison-Wesley Publishing Co., Inc., Reading, Mass., 1980.)

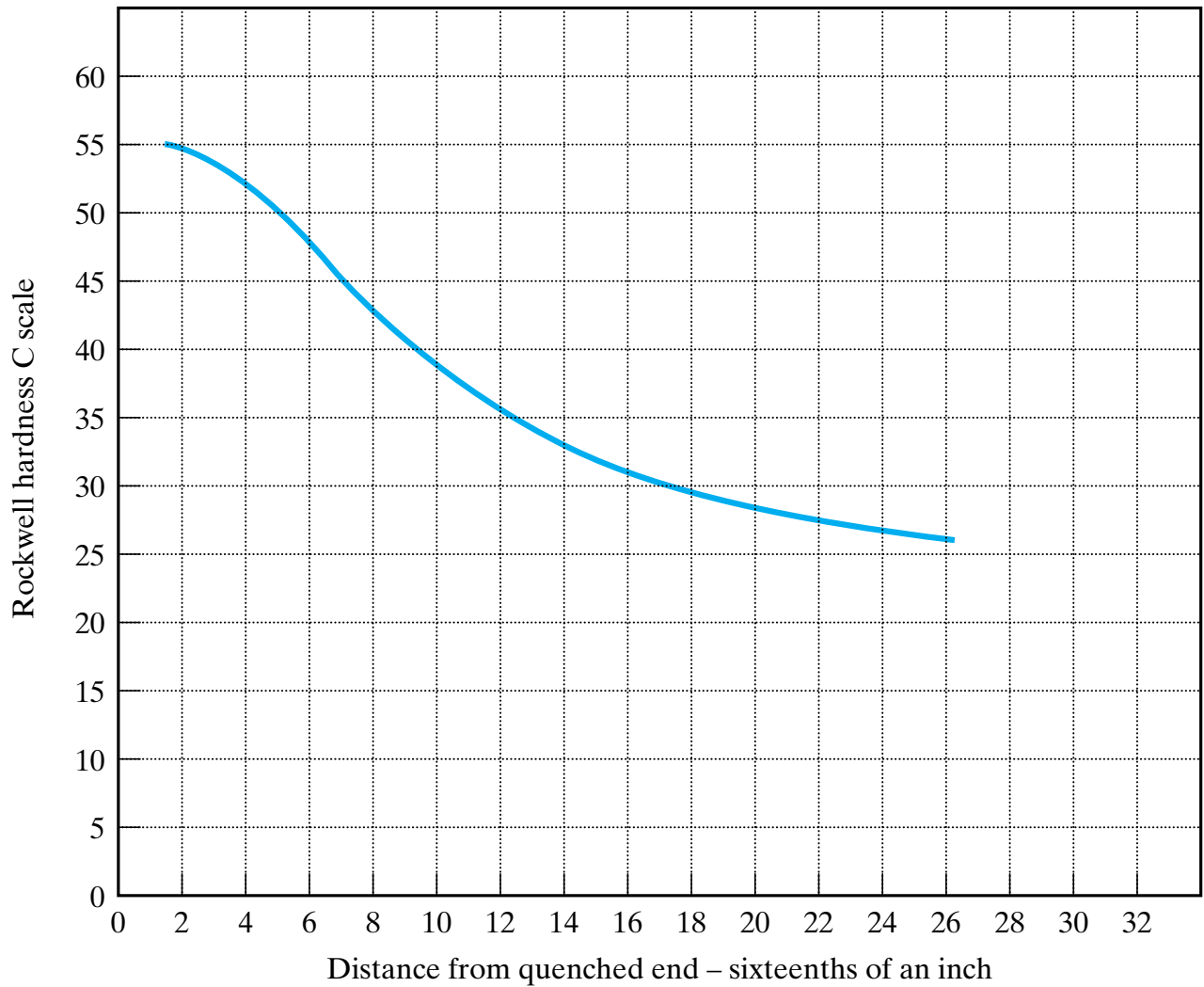


**Figure 10-23** Variation in hardness along a typical Jominy bar. (From W. T. Lankford et al., Eds., *The Making, Shaping, and Treating of Steel, 10th Ed.*, United States Steel, Pittsburgh, Pa., 1985. Copyright 1985 by United States Steel Corporation.)

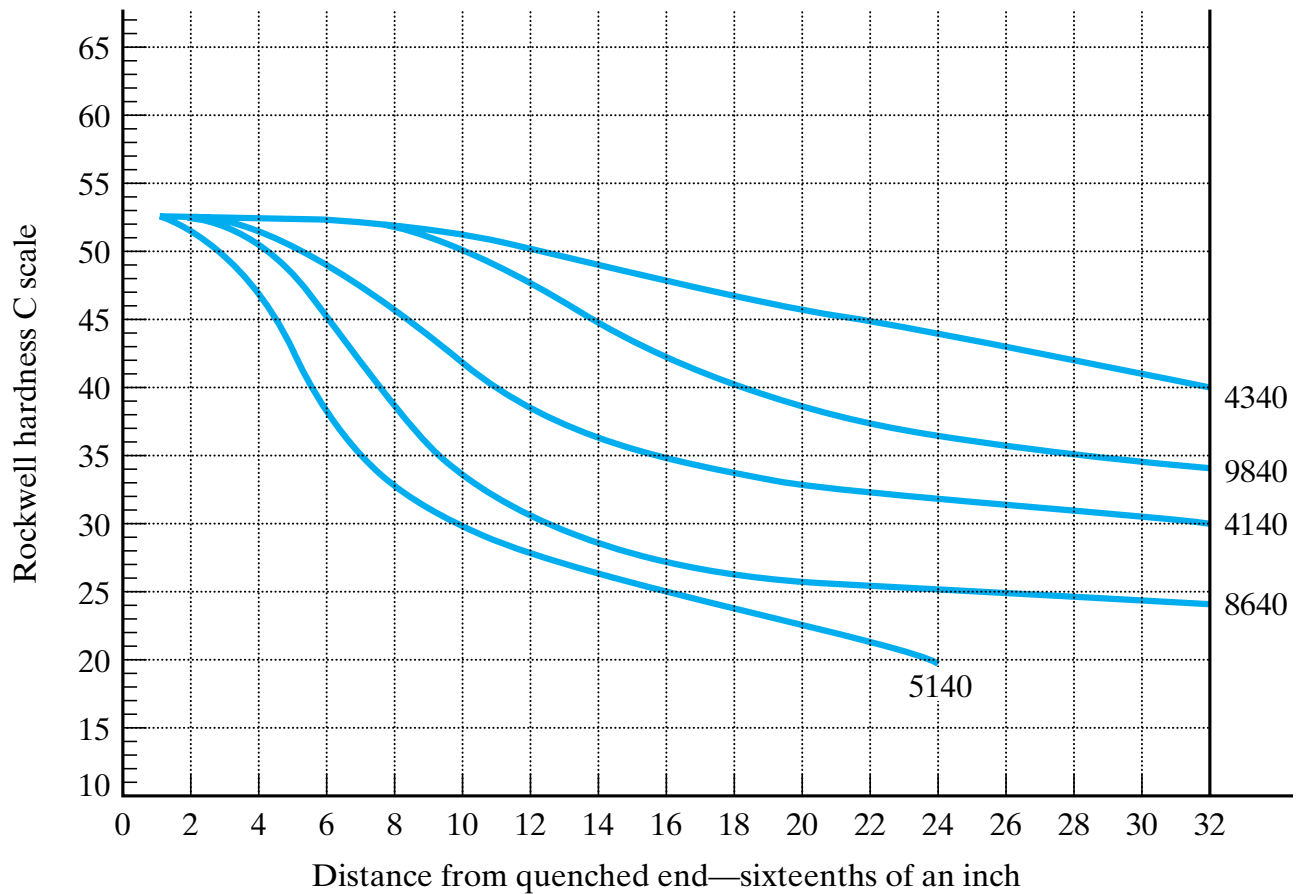


**Figure 10-24** Hardenability curves for various steels with the same carbon content (0.40 wt %) and various alloy contents. The codes designating the alloy compositions are defined in Table 11.1. (From W. T. Lankford et al., Eds., *The Making, Shaping, and Treating of Steel, 10th Ed.*, United States Steel, Pittsburgh, Pa., 1985. Copyright 1985 by United States Steel Corporation.)

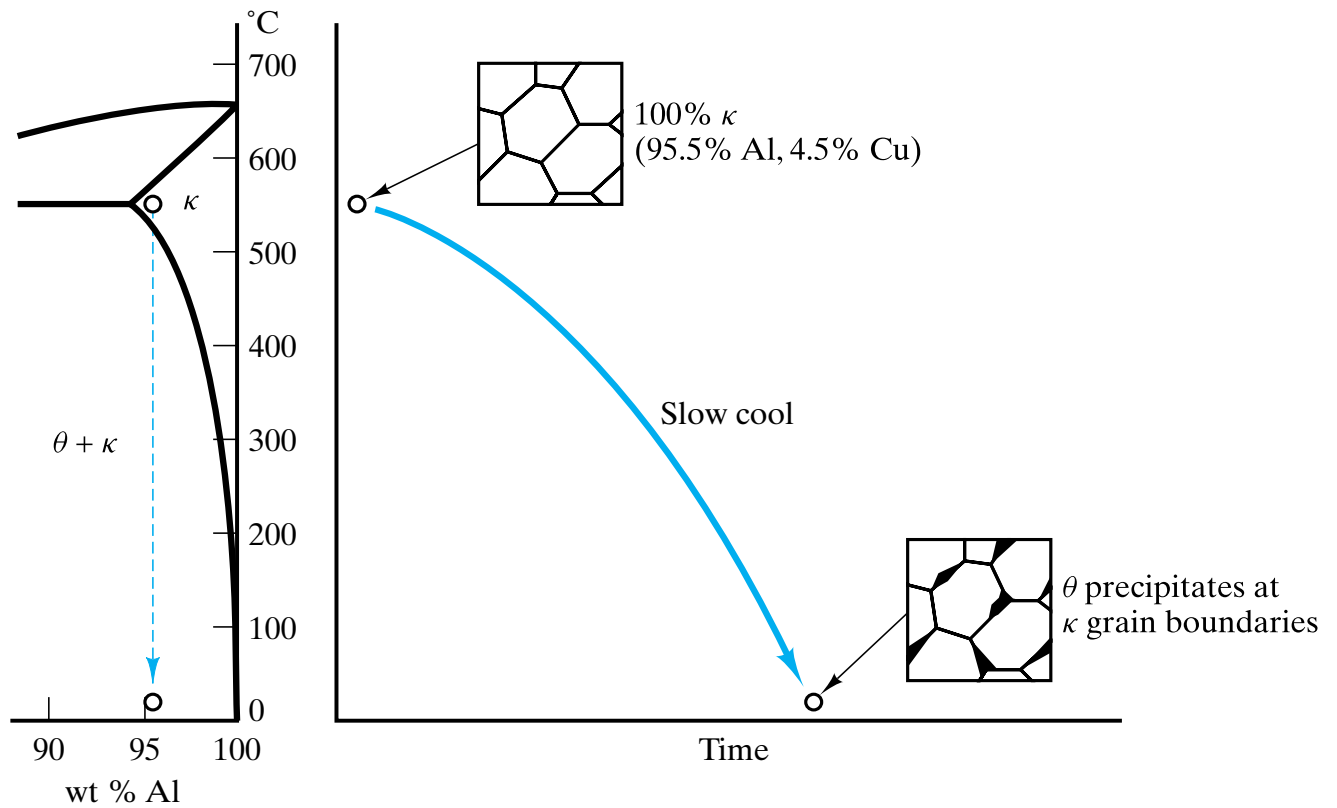


**Figure 10-25** Coarse precipitates form at grain boundaries in an Al–Cu (4.5 wt %) alloy when slowly cooled from the single-phase ( $\kappa$ ) region of the phase diagram to the two-phase ( $\theta + \kappa$ ) region. These isolated precipitates do little to affect alloy hardness.

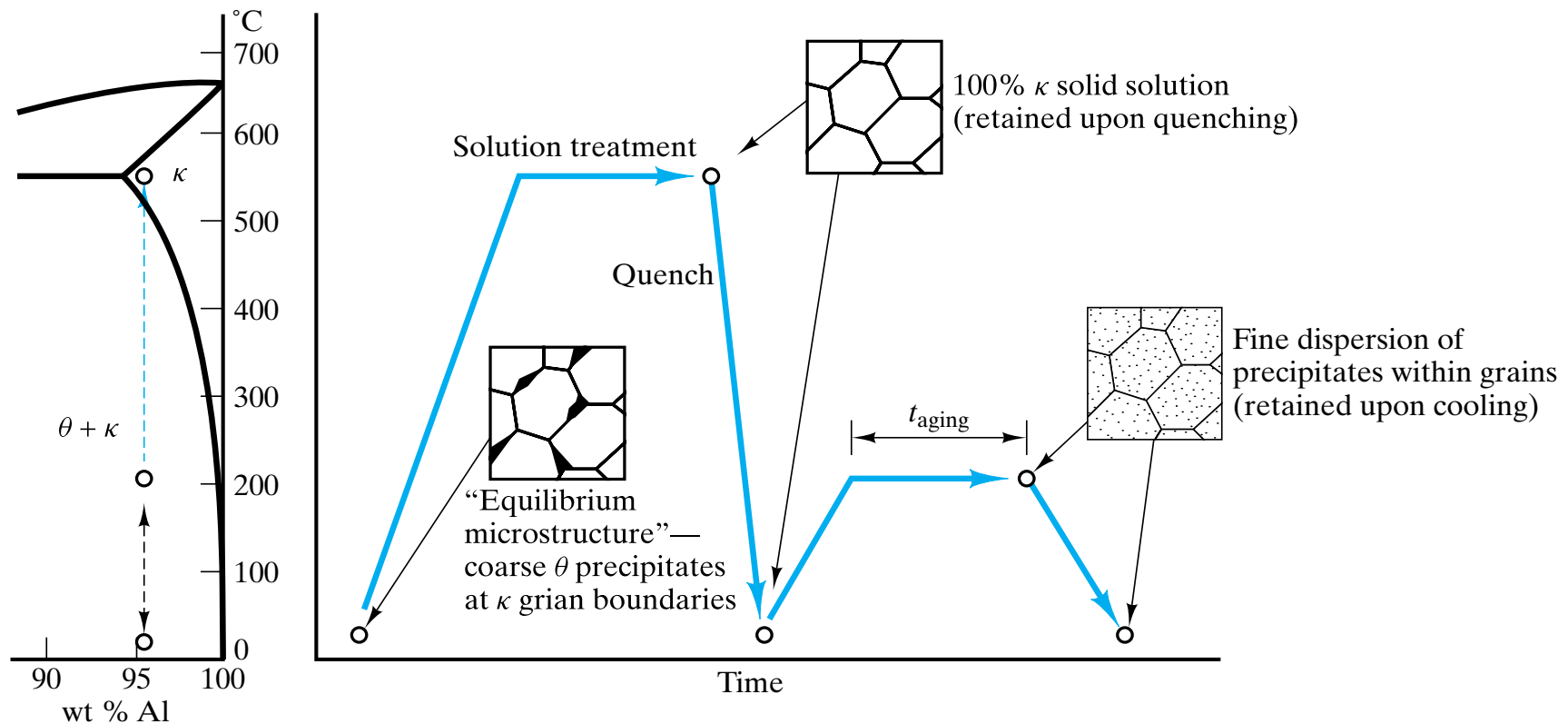


**Figure 10-26** By quenching and then reheating an Al–Cu (4.5 wt %) alloy, a fine dispersion of precipitates forms within the  $\kappa$  grains. These precipitates are effective in hindering dislocation motion and, consequently, increasing alloy hardness (and strength). This is known as precipitation hardening, or age hardening.

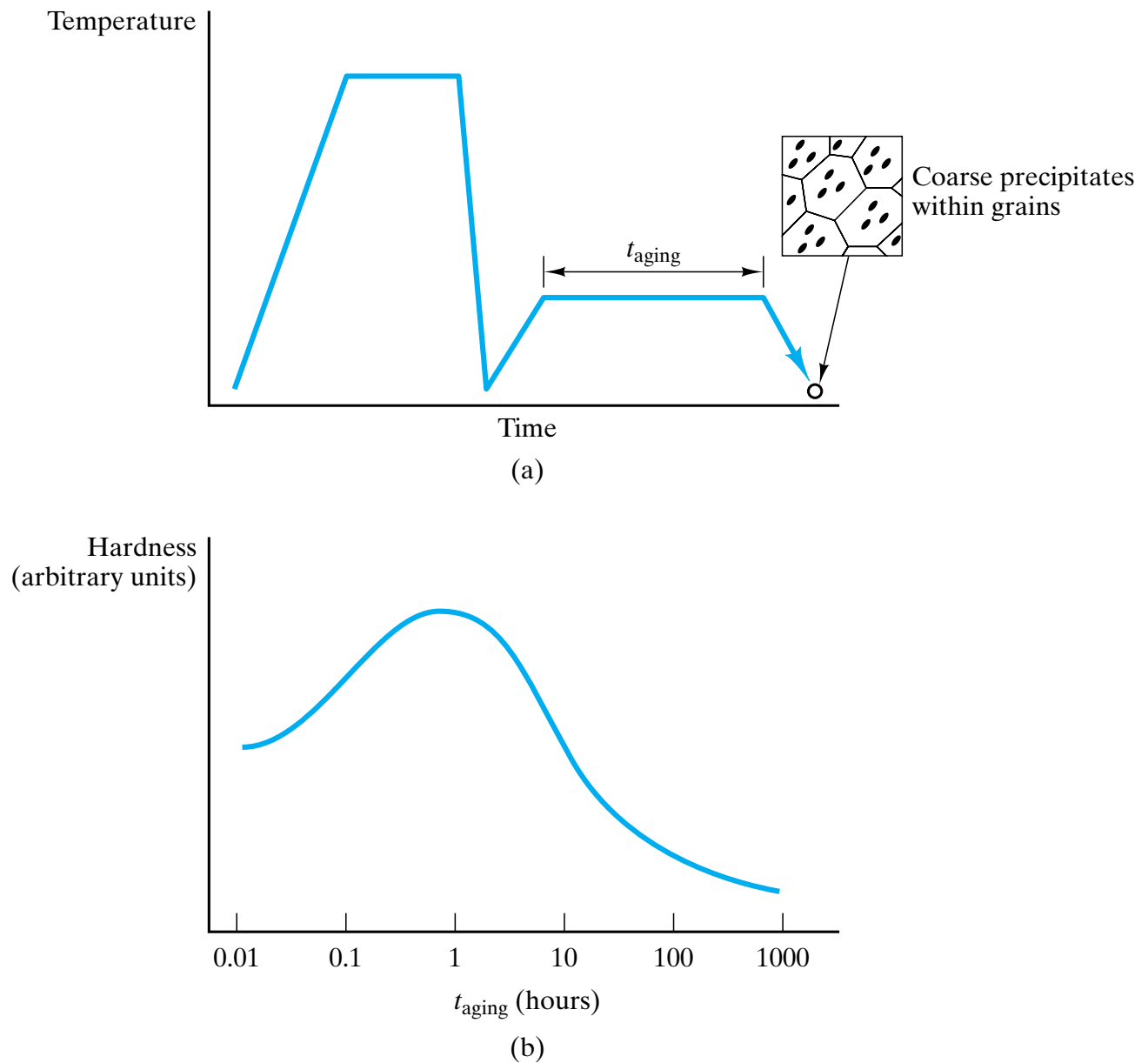


**Figure 10-27** (a) By extending the reheat step, precipitates coalesce and become less effective in hardening the alloy. The result is referred to as “overaging.” (b) The variation in hardness with the length of the reheat step (“aging time”).

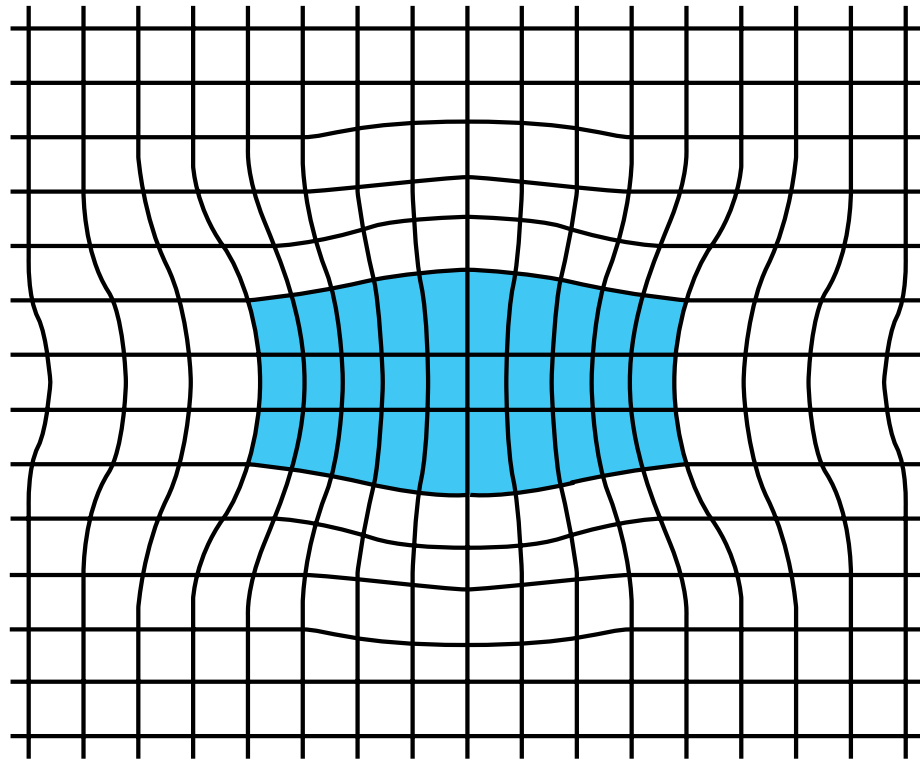


**Figure 10-28** Schematic illustration of the crystalline geometry of a Guinier–Preston (G.P.) zone. This structure is most effective for precipitation hardening, and is the structure developed at the hardness maximum in Figure 10–27b. Note the coherent interfaces lengthwise along the precipitate. The precipitate is approximately  $15\text{ nm} \times 150\text{ nm}$ . (From H. W. Hayden, W. G. Moffatt, and J. Wulff, *The Structure and Properties of Materials, Vol. 3: Mechanical Behavior*, John Wiley & Sons, Inc., New York, 1965.)

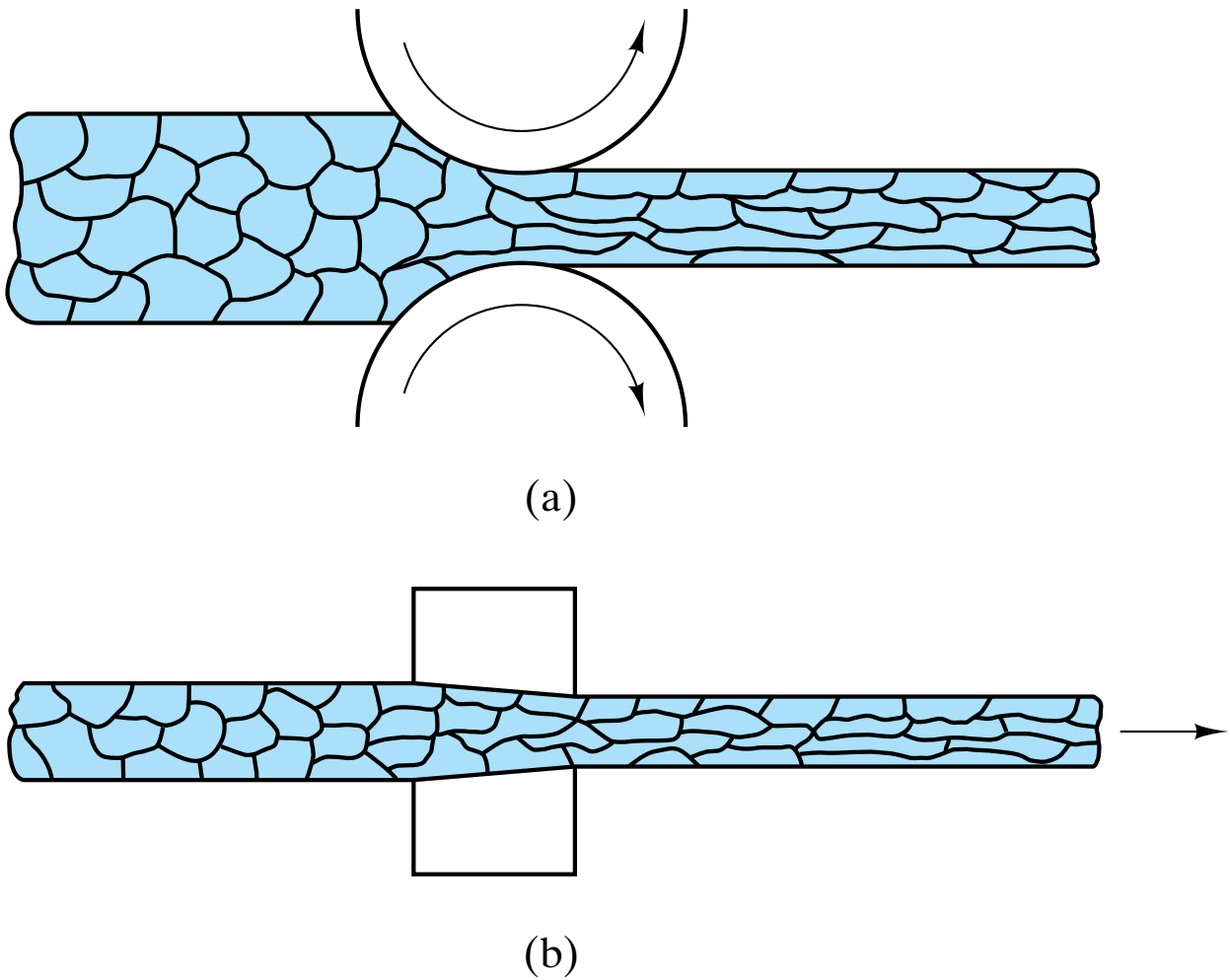
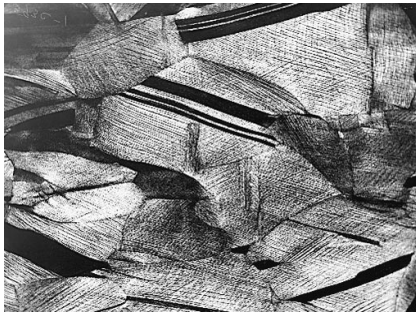


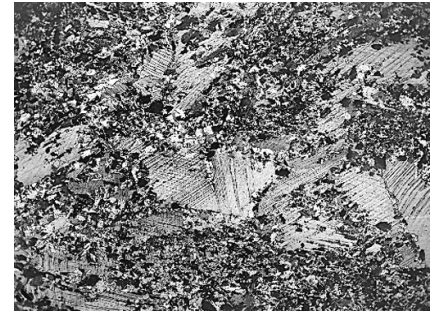
**Figure 10-29** Examples of cold-working operations: (a) cold-rolling of a bar or sheet and (b) cold-drawing a wire. Note in these schematic illustrations that the reduction in area caused by the cold-working operation is associated with a preferred orientation of the grain structure.



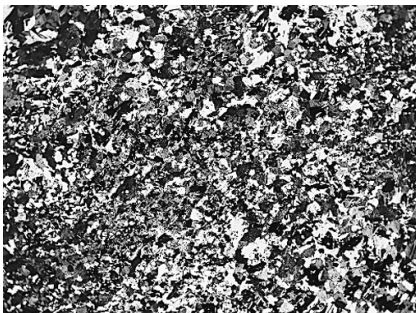
(a)



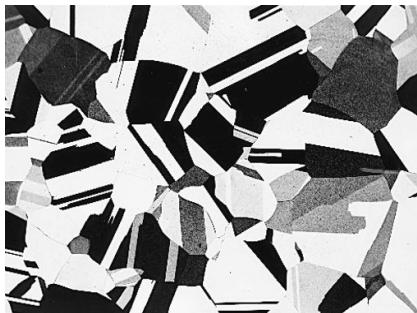
(b)



(c)

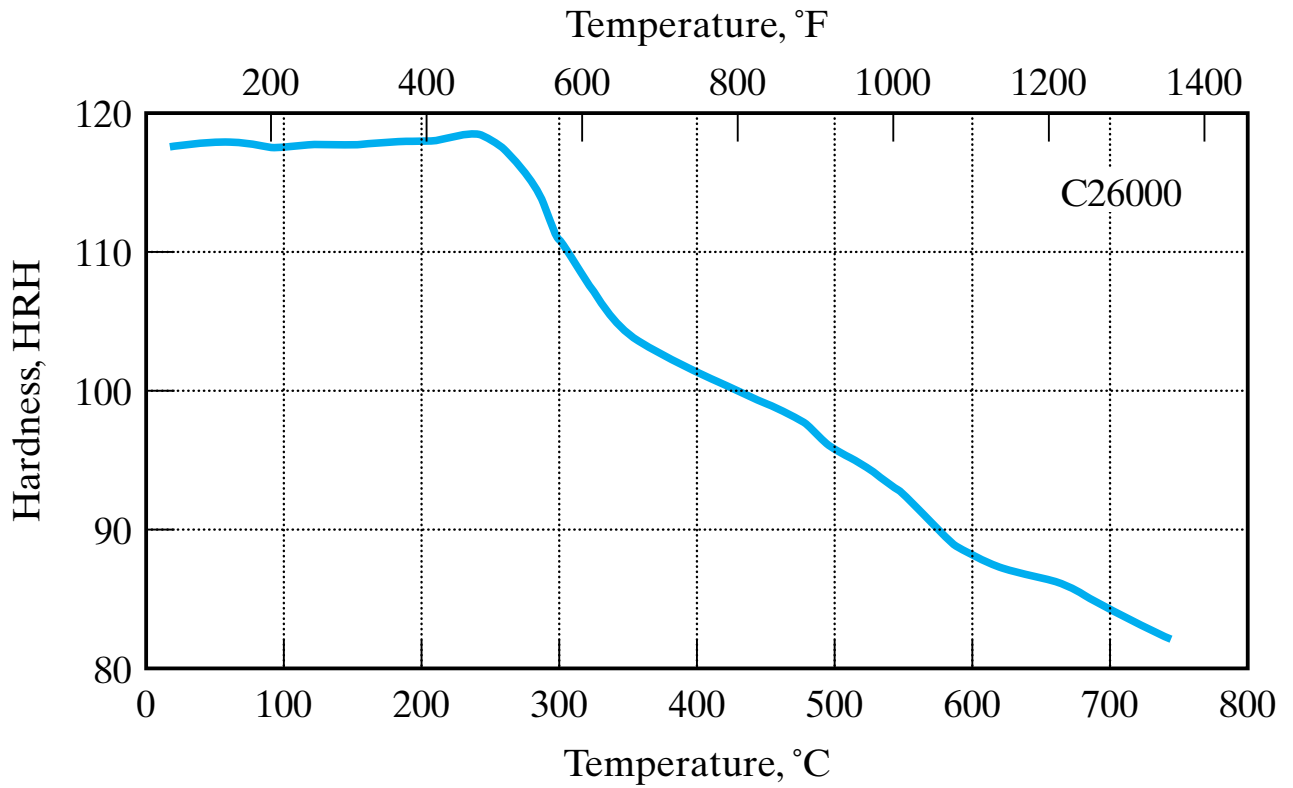


(d)

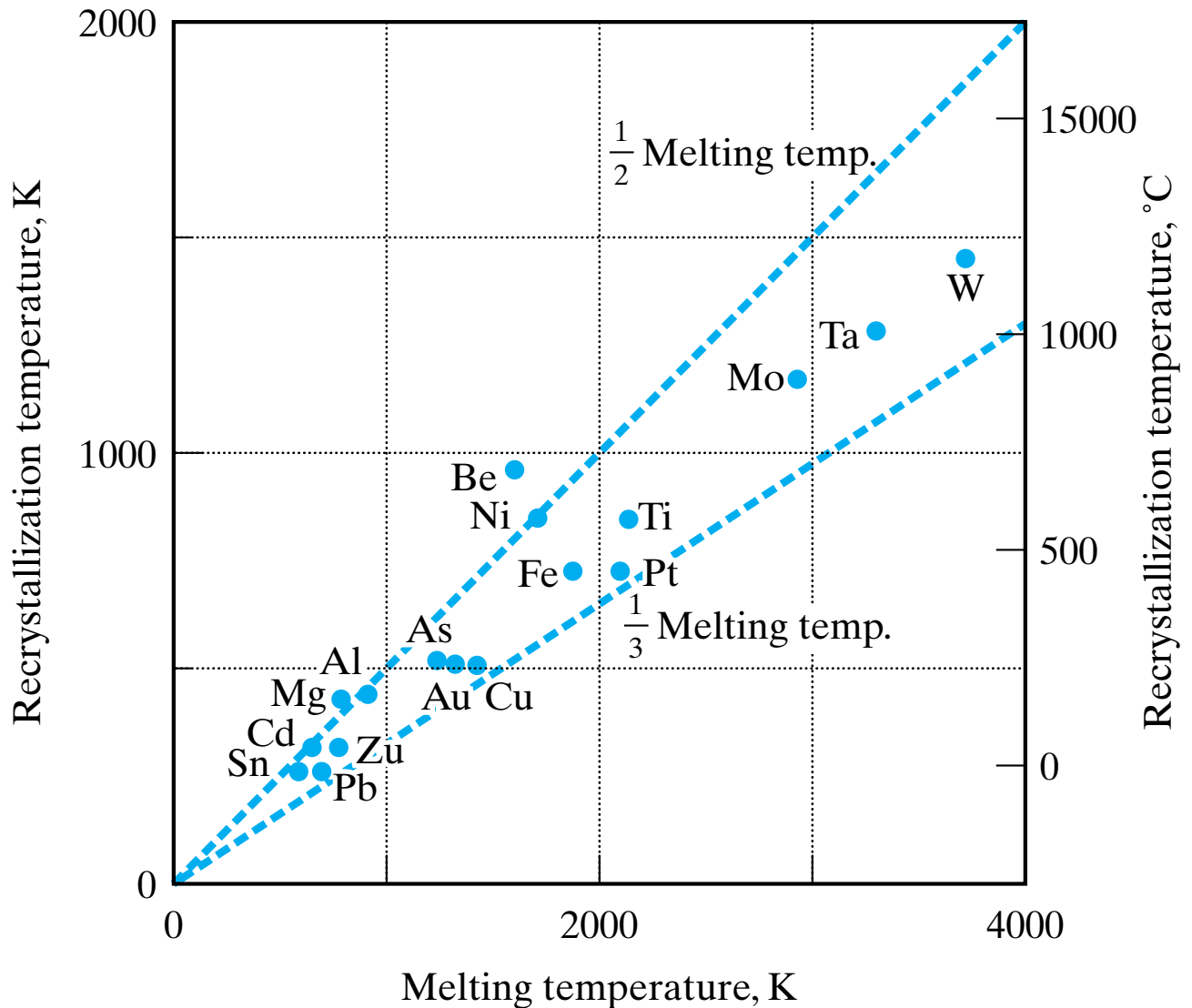


(e)

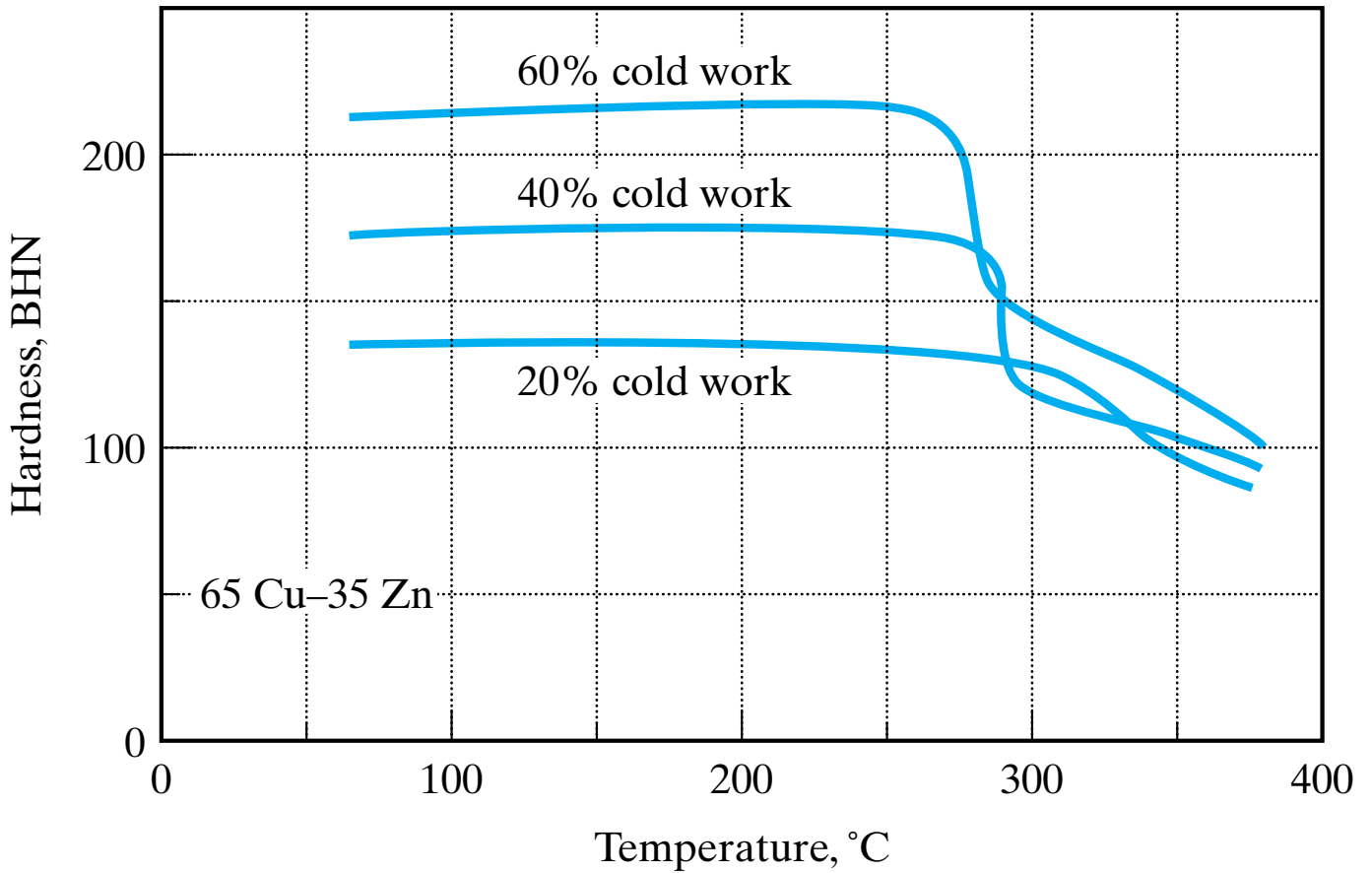
**Figure 10-30** *Annealing can involve the complete recrystallization and subsequent grain growth of a cold-worked microstructure. (a) A cold-worked brass (deformed through rollers such that the cross-sectional area of the part was reduced by one-third). (b) After 3 s at 580° C, new grains appear. (c) After 4 s at 580° C, many more new grains are present. (d) After 8 s at 580° C, complete recrystallization has occurred. (e) After 1 h at 580° C, substantial grain growth has occurred. The driving force for this is the reduction of high-energy grain boundaries. The predominant reduction in hardness for this overall process had occurred by step (d). All micrographs at magnification of 75 ×. (Courtesy of J. E. Burke, General Electric Company, Schenectady, N.Y.)*



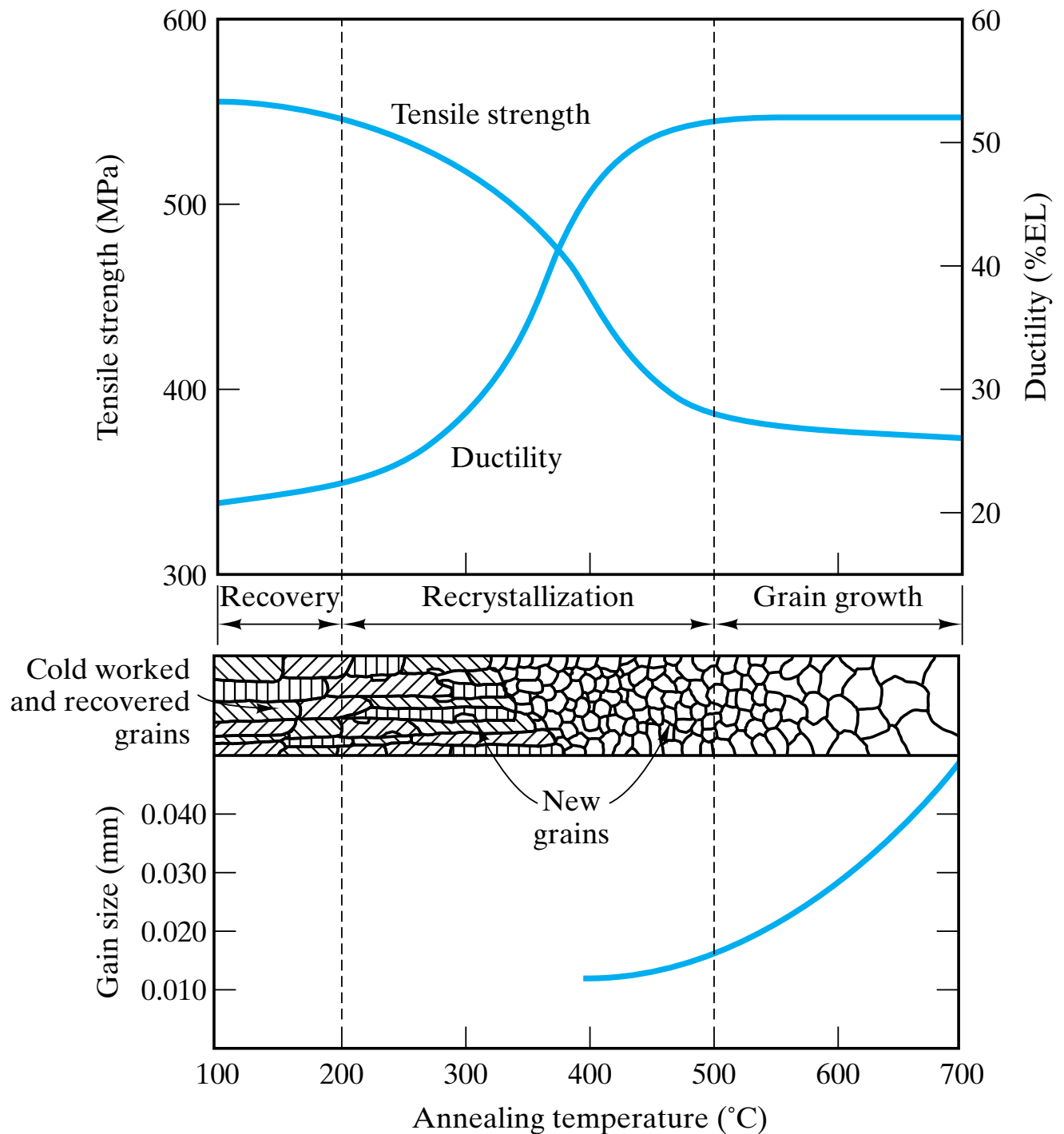
**Figure 10-31** The sharp drop in hardness identifies the recrystallization temperature as  $\sim 290^{\circ}\text{C}$  for the alloy C26000, “cartridge brass.” (From *Metals Handbook, 9th Ed., Vol. 4, American Society for Metals, Metals Park, Ohio, 1981.*)



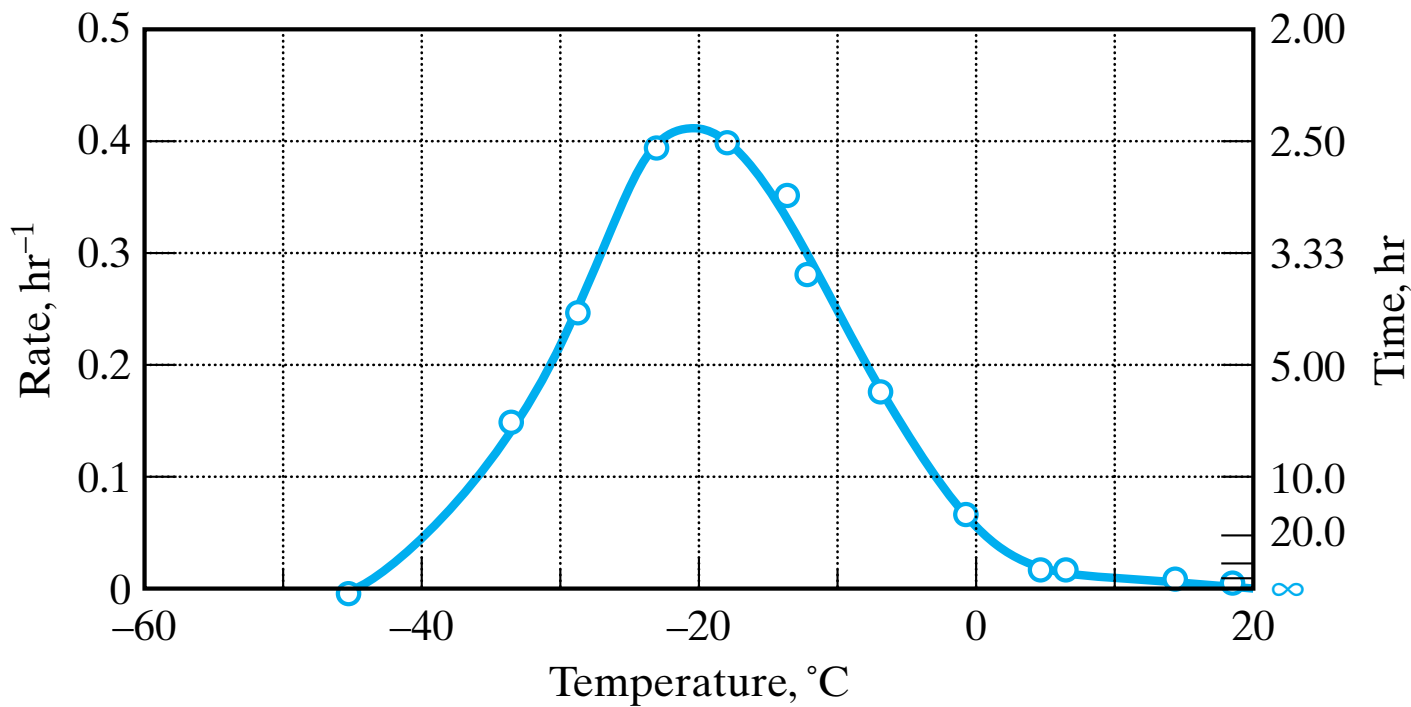
**Figure 10-32** Recrystallization temperature versus melting points for various metals. This plot is a graphic demonstration of the rule of thumb that atomic mobility is sufficient to affect mechanical properties above approximately  $\frac{1}{3}$  to  $\frac{1}{2}T_m$  on an absolute temperature scale. (From L. H. Van Vlack, *Elements of Materials Science and Engineering, 3rd Ed.*, Addison-Wesley Publishing Co., Inc., Reading, Mass, 1975.)



**Figure 10-33** For this cold-worked brass alloy, the recrystallization temperature drops slightly with increasing degrees of cold work. (From L. H. Van Vlack, *Elements of Materials Science and Engineering, 4th Ed.*, Addison-Wesley Publishing Co., Inc., Reading, Mass. 1980.)

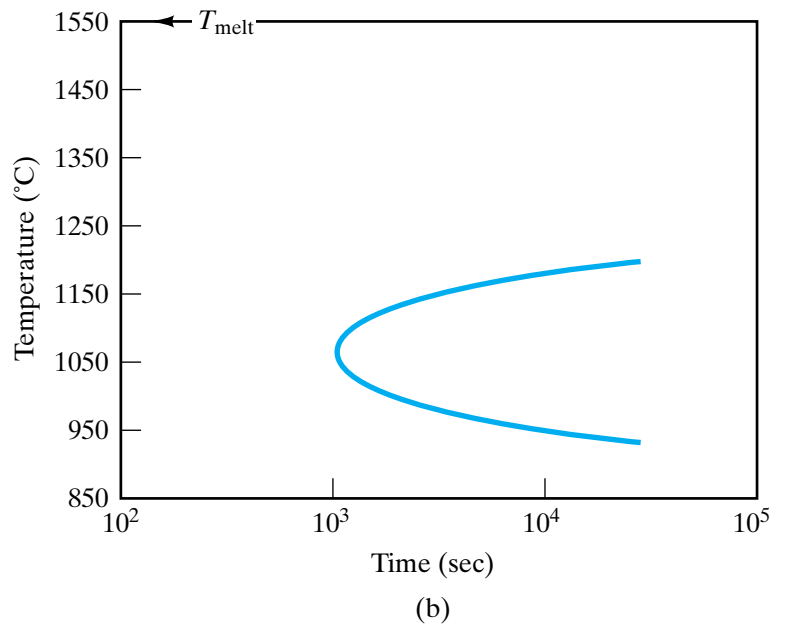
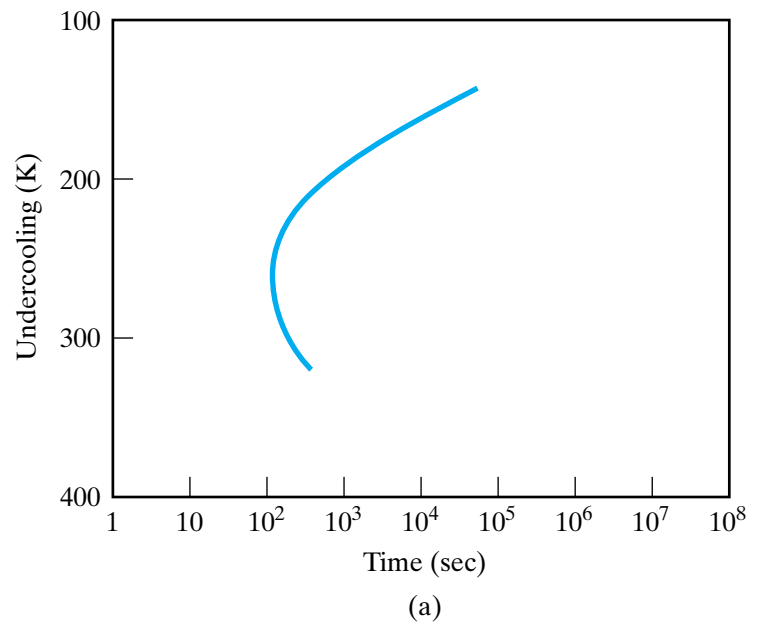


**Figure 10-34** Schematic illustration of the effect of annealing temperature on the strength and ductility of a brass alloy shows that most of the softening of the alloy occurs during the recrystallization stage. (After G. Sachs and K. R. Van Horn, *Practical Metallurgy: Applied Physical Metallurgy and the Industrial Processing of Ferrous and Nonferrous Metals and Alloys*, American Society for Metals, Cleveland, Ohio, 1940.)



**Figure 10-35** Rate of crystallization of rubber as a function of temperature. (From L. A. Wood, in H. Mark and G. S. Whitby, Eds., *Advances in Colloid Science*, Vol. 2, Wiley Interscience, New York, 1946, pp. 57–95.)

**Figure 10-36** TTT diagram for (a) the fractional crystallization ( $10^{-4}$  vol %) of a simple glass of composition  $\text{Na}_2\text{O} \cdot 2\text{SiO}_2$  and (b) the fractional crystallization ( $10^{-1}$  vol%) of a glass of composition  $\text{CaO} \cdot \text{Al}_2\text{O}_3 \cdot 2\text{SiO}_2$ . [Part (a) from G. S. Meiling and D. R. Uhlmann, Phys. Chem. Glasses 8, 62 (1967) and part (b) from H. Yinnon and D. R. Uhlmann, in Glass: Science and Technology, Vol. 1, D. R. Uhlmann and N. J. Kreidl, Eds., Academic Press, New York, 1983, pp. 1–47.]



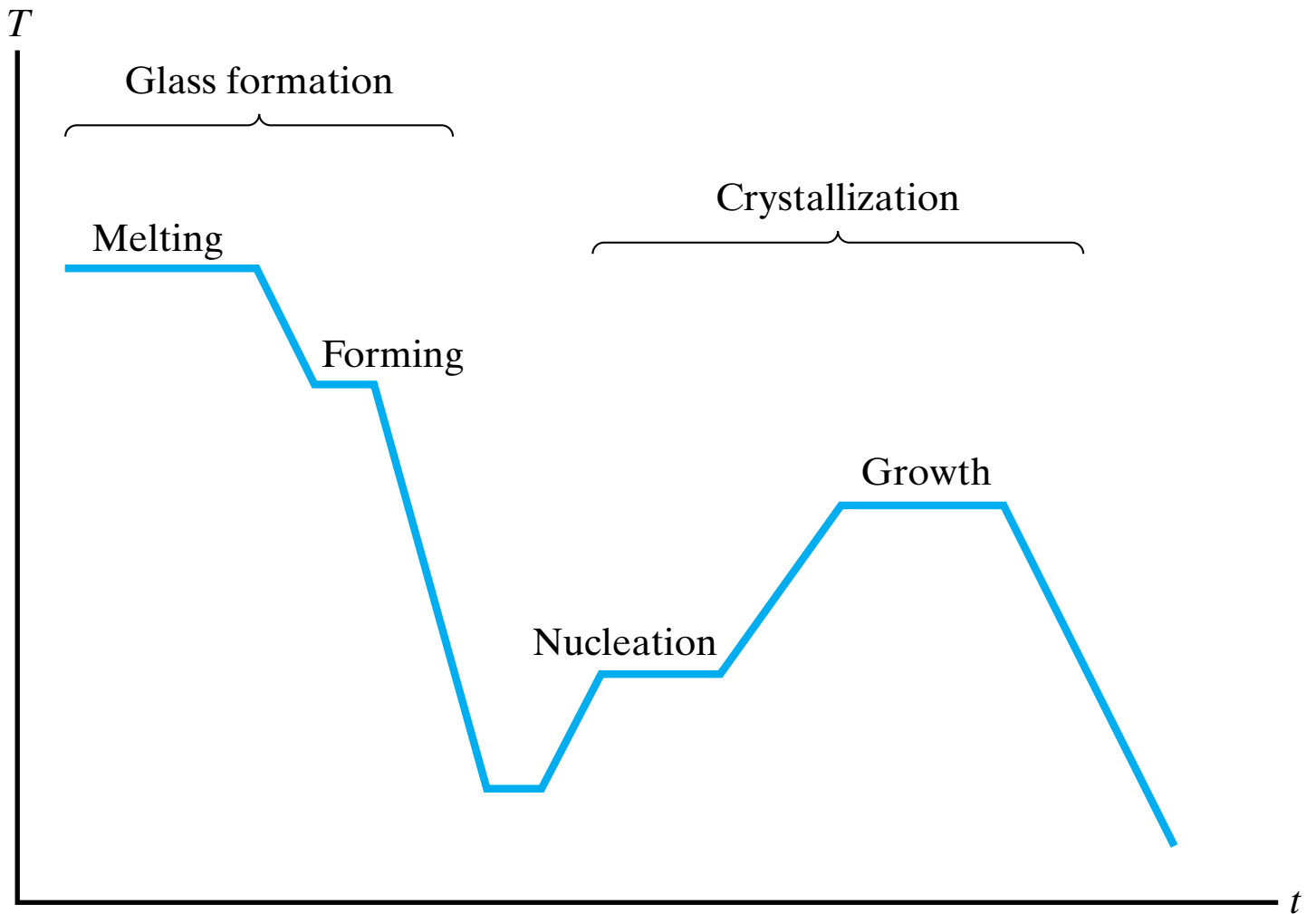


**Figure 10-37** Typical thermal history for producing a glass ceramic by the controlled nucleation and growth of crystalline grains.

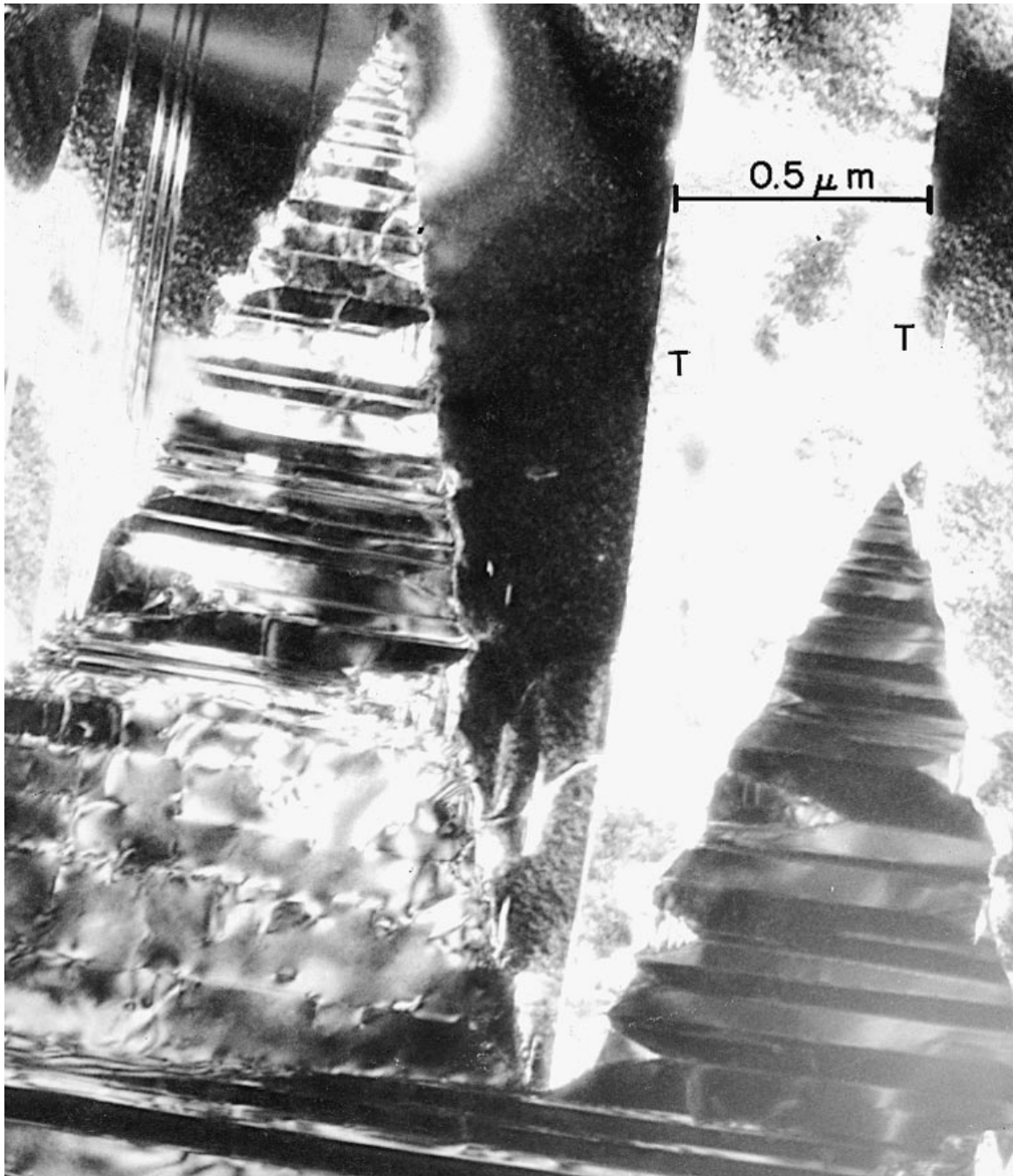


**Figure 10-38** *Transmission electron micrograph of monoclinic zirconia showing a microstructure characteristic of a martensitic transformation. Included in the evidence are twins labeled T. See Figure 4-15 for an atomic-scale schematic of a twin boundary and Figure 10-13 for the microstructure of martensitic steel. (Courtesy of Arthur H. Heuer)*

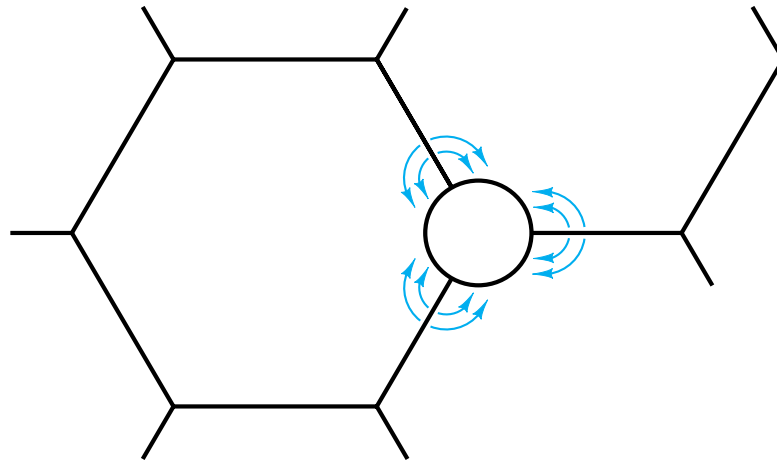


**Figure 10-39** *An illustration of the sintering mechanism for shrinkage of a powder compact is the diffusion of atoms away from the grain boundary to the pore, thereby “filling in” the pore. Each grain in the microstructure was originally a separate powder particle in the initial compact.*

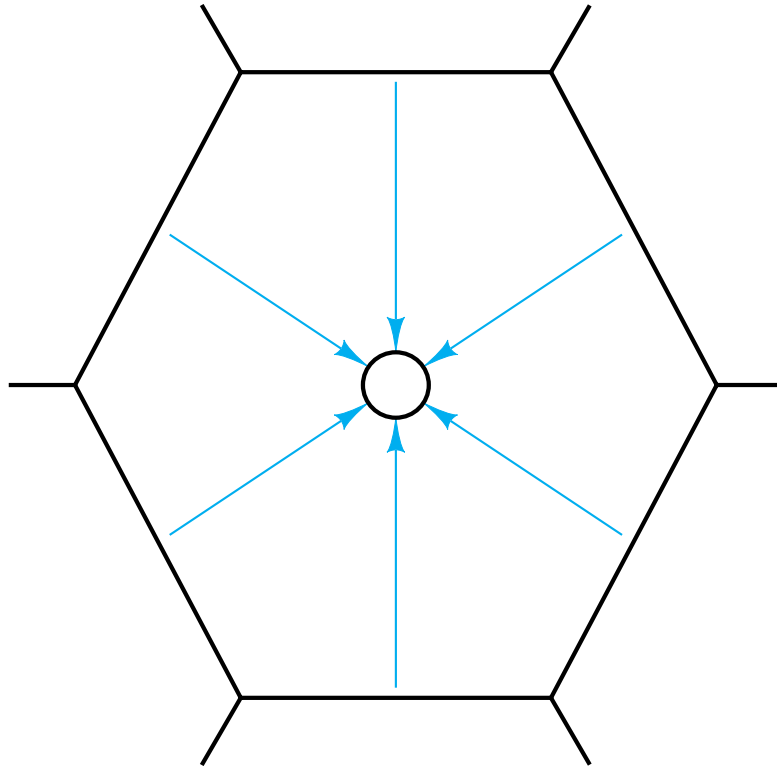


**Figure 10-40** *Grain growth hinders the densification of a powder compact. The diffusion path from grain boundary to pore (now isolated within a large grain) is prohibitively long.*